Solidification dynamics of three-phased eutectic patterns in 2D

by

Sinan Yücetürk

A Thesis Submitted to the
Graduate School of Sciences and Engineering
in Partial Fulfillment of the Requirements for
the Degree of

Master of Science
in
Mechanical Engineering

Koc University

August 2015

Koc University

Graduate School of Sciences and Engineering

This is to certify that I have examined this copy of a master's thesis by

Sinan Yücetürk

and have found that it is complete and satisfactory in all respects,
and that any and all revisions required by the final
examining committee have been made.

Committee Members:

_____

Melis Şerefoğlu Kaya, Ph. D. (Advisor)

_____

Sabine Bottin-Rousseau, Ph. D.

_____

Murat Sözer, Ph. D.

Date: _____

ABSTRACT

Materials select particular growth patterns during solidification depending on the crystalline nature of phases as well as external parameters such as cooling rate, composition, and sample dimensions. Although one cannot change the nature of phases, solidification dynamics can be altered by changing the external parameters in order to understand and control the microstructural features of solidified materials. Controlling these features is highly critical since the material properties including mechanical, physical, and electrical properties are extremely dependent on the microstructure of the materials. Among these solidification patterns, alloys forming eutectic patterns are used extensively in industry in a wide range of processes such as casting, welding, and soldering of engineered components due to their favorable properties resulting from their micro-composite structure.

The majority of the eutectic solidification studies in the literature focus on two-phased eutectic systems where there is only one possible arrangement of phases (the ABAB order), due to their simplicity compared to higher-order systems. However, in pursuit of new generations of materials, alloys obtained using ternary, quaternary, and even higher order systems, have been extensively used in the industry. With the advent of the third phase, the number of possible arrangements of phases and spacing adjustment mechanisms increase tremendously. In this thesis, the growth dynamics of In-Bi-Sn three-phased eutectic system is investigated experimentally using real-time directional solidification technique and 2D samples at the ternary eutectic composition.

The stable microstructure formed in three-phased eutectics is found to grow with ABAC stacking order, where A, B, and C stand for individual lamella of the In_2Bi, β-In, and γ-Sn phases, respectively. This ABAC order is not only stable in the basic state, but also in tilted and asymmetric patterns. At a given growth velocity *V*, ABAC pattern is observed to be stable over a finite range of eutectic spacing, similar to binary eutectic microstructures. When the stable ABAC pattern is perturbed enough by changing the growth velocity, it is forced to go beyond the stability limits and as a result, the system employs spacing adjustment mechanisms like elimination, oscillation, and branching to go back to the stable regime. Beyond the upper limit of the stability, branching takes place, which is systematically preceded by the amplification of a period-preserving oscillatory mode (1λO) that has been predicted by phase-field simulations of a three-phased eutectic system [1]. However, in this study, oscillations were never observed to grow at steady-state, but they were transients that

are either amplified or damped. Beyond the lower stability limit, the system eliminates a complete ABAC pattern where at two-phased eutectics only an A or B phase is eliminated at spacing values below the lower limit. Additionally, the elimination mechanism observed in the two-phased eutectics is Eckhaus instability, whereas for three-phased eutectics the requirements of Eckhaus instability are found to be invalid. The lower stability limit for three-phased eutectics is measured to be substantially lower than the minimum undercooling spacing which is consistent with binary eutectic systems. The scaling constant [2] of ABAC pattern is found as $\lambda_{JH}^2 V = 135 \pm 35$ μm^3/s. The upper and lower limits of stability for ABAC pattern are found as $\Lambda_{br} = 1.9 \pm 0.5$ and $0.6 < \Lambda_c < 1.1$, respectively, where Λ is normalized eutectic spacing with respect to minimum undercooling spacing (λ_{JH}). Finally, some observations of more complex patterns (ex: ABABACACAC), tilted patterns, and thickness-asymmetry in In_2Bi phases are reported.

ÖZET

Malzemeler katılaştırma esnasında fazların kristal yapıları yanı sıra soğuma hızı, kompozisyon, ve numune boyutu gibi dış parametrelere de bağlı olarak belirli büyüme dizilimleri gösterirler. Fazların kristal yapılarının değiştirilememesine karşın, dış etmenler değiştirilerek katılaştırma dinamikleri farklılaştırılıp mikroyapının nasıl oluştuğu anlaşılabilir ve böylelikle katılaşma sonucu elde edilen malzemelerin mikroyapıları kontrol edilebilir. Mikroyapıları kontrol edebilmek çok önemli, çünkü malzemelerin mekanik, fiziksel ve elektriksel özellikleri gibi bir çok özelliği mikroyapılarına oldukça bağlıdır. Katılaştırma mikroyapıları arasında bulunan ötektik malzemeler, mikro-kompozit yapılarından dolayı iyi malzeme özellikleri sunan alaşımlardır ve döküm, kaynak ve lehim gibi bir çok üretim yöntemlerinde kullanılan mühendislik malzemeleridir.

Literatürde, ötektik katılaştırma üzerine yapılmış çalışmaların büyük çoğunluğu yalnızca tek bir olası büyüme dizilimine (ABAB dizilimi) sahip olan ikili ötektik sistemler ile yapılmıştır ve bunun başlıca nedeni iki-fazlı ötektik sistemlerin katılaşma dinamiklerinin anlaşılmasının, üç ve daha çok fazlı sistemlerle kıyaslandığında çok daha basit olmalarındandır. , Fakat diğer bir yandan, yeni malzemeler keşfetme yolunda, üç ve daha çok fazlı sistemler kullanılarak elde edilen alaşımlar endüstride yaygın olarak kullanılmaktadır. Üçüncü fazın eklenmesi ile olası büyüme dizilimlerinin ve ötektik mesafesi ayarlamasında kullanılan mekanizmaların sayısı çok büyük oranda artmaktadır. Bu tezde, In-Bi-Sn üç fazlı ötektik sisteminin katılaştırma dinamikleri gerçek zamanlı tek yönlü katılaştırma yöntemi ve ötektik kompozisyona sahip 2B numuneler kullanarak incelenmiştir.

Üç-fazlı ötektik sistemlerde kararlı halde büyüyen periyodik mikroyapının ABAC diziliminde olduğu belirlenmiştir. Bu dizilimde A, B, ve C sırasıyla In_2Bi, β-In, ve γ-Sn fazlarını ifade etmektedir. ABAC diziliminin, yalnızca temel durumda değil, eğimli ve asimetrik yapılarda da kararlı olduğu görülmüştür. Sabit bir katılaştırma hızında V, ABAC diziliminin sadece belirli bir ötektik mesafe aralığında kararlı halde büyüyebildiği gözlemlenmiştir, ki bu açıdan iki-fazlı ötektik sistemlere benzerdirler. Kararlı halde bulunan ABAC dizilimine sahip mikroyapının, katılaştırma hızı yeterince değiştirilerek kararlılık limitleri dışına çıkmaya zorlandığında eliminasyon, osilasyon, ve dallanma gibi mesafe ayarlama mekanizmaları kullanarak tekrar kararlı hale geldiği görülmüştür. Sistemde, kararlılığın üst sınırı geçildiğinde dallanma mekanizması ve her bir dallanmadan öncede,

sistematik olarak, bir ötektik mesafesinde kendisini tekrar eden (1λO) osilasyon mekanizması gözlemlenmiştir. Bu osilasyon mekanizması, üç-fazlı ötektik bir sistem kullanılarak elde edilen faz-alanı simülasyonları sonuçlarında da gözlemlenmiştir [1]. Ancak bu çalışmada, osilasyonların kararlı bir şekilde büyümediği, giderek genişleyen veya sönümlenen geçiş mekanizmaları olduğu belirlenmiştir. Kararlılığın alt limiti geçildiğinde ise sistem, iki fazlı sistemlerde sadece A ya da B fazlarından birini elimine edilirken, üç fazlı ötektiklerde ABAC dizilimindeki her bir fazı teker teker elimine etmektedir. Ayrıca, iki-fazlı sistemlerde görülen eliminasyon mekanizması Eckhaus kararsızlığı iken, bir eliminasyonun Eckhaus kararsızlığı olarak tanımlanması için gereken koşullar üç-fazlı sistemlerde sağlanamamaktadır. Üç-fazlı ötektiklerde, iki-fazlılarda da görüldüğü gibi, kararlılık alt limitinin minimum ötektik mesafesi değerinden düşük değerde olduğu belirlenmiştir. ABAC diziliminin ötektik mesafe sabiti [2] $\lambda_{JH}^2 V$ = 135 $\pm$ 35 μ m^3/s, üst ve alt kararlılık limitleri ise sırasıyla Λ_{br} = 1.9 ± 0.5 ve 0.6 < Λ_c < 1.1 olarak belirlenmiştir. Λ değeri, minimum ötektik mesafesine (λ_{JH}) göre normalize edilmiş ötektik mesafesidir. Son olarak, bu tezde deneyler sırasında gözlemlenen daha kompleks dizilimler (örn. ABABACACAC), eğimli yapılar ve In_2Bi fazlarının kalınlık asimetrisi gibi mikroyapısal oluşumlar sunulmaktadır.

ACKNOWLEDGEMENTS

I would like to express the deepest appreciation to my advisor Melis Şerefoğlu Kaya who has the approach and the excellence of a genius along with a friendly hearth: she continually conveyed a spirit of determination in regard to science and research, and an excitement in regard to teaching. This dissertation would not have been possible without her guidance and persistent help. I am indebted to her for her understanding, wisdom, patience, enthusiasm and encouragement for pushing me farther than I thought I could go.

I also would like to thank my committee member, Sabine Bottin-Rousseau, our collaborator in Paris. When I was in Paris Institute of Nanosciences (INSP) to be able to conduct experimental studies for this thesis, Sabine became the greatest host and excellent teacher to me. Also, I sincerely thank to Murat Sözer since he accepted to come to my thesis committee in his busy schedule.

I should especially thank to my family for the words of encouragement and the help not to give up. To my group mate Samira Mohagheghi for her contributions to this dissertation. To my friends Yaprak Özbakır, Volkan Balcı, Göktuğ Gönel, Günce Cinay, Erdal Aydın, and Ehsan Sarayloo for their supports and for the fun they brought to my life in İstanbul. Finally, I thank to my darling, Tuğçe Zorlu, for the everlasting support and kindness during the writing procedure of this thesis.

This project was funded by TUBITAK 3501 (Grant no: 212M013) and European Commission Marie Curie Career Integration Grant FP7-PEOPLE-2012-CIG (NEUSOL – 334216). I thank our collaborators INSP-UPMC-CNRS team in France and ACCESS team in Germany for their contributions to this study.

TABLE OF CONTENTS

LIST OF TABLES

LIST OF FIGURES

NOMENCLATURE

ΔT	undercooling
K_r	growth constant for eutectics in diffusion undercooling term
K_c	growth constant for eutectics in curvature undercooling term
V	growth velocity
λ	eutectic spacing
λ_m, λ_{JH}	minimum undercooling spacing, Jackson-Hunt eutectic spacing
G	thermal gradient
T_E	eutectic temperature
C_E	eutectic composition
V_0	initial velocity
V_1	final velocity
D_λ	phase diffusion coefficient
λ_0	average eutectic spacing
$A(t)$	time dependent amplitude value
A_0	amplitude value of best fit
σ	standard deviation
t	time
t_0	time at the maximum spacing modulation
k	wavevector
L	length of the spacing modulation
λ_c	lower critical eutectic spacing (elimination)
λ_{br}	upper critical eutectic spacing (branching)
B	material dependent constant
$\Lambda_0 = \frac{\lambda_0}{\lambda_{JH}}$	normalized average eutectic spacing
$\Lambda_c = \frac{\lambda_c}{\lambda_{JH}}$	normalized lower critical eutectic spacing (elimination)
$\Lambda_{br} = \frac{\lambda_{br}}{\lambda_{JH}}$	normalized upper critical eutectic spacing (branching)
$\Lambda_{osc} = \frac{\lambda_{osc}}{\lambda_{JH}}$	normalized critical eutectic spacing (oscillation)

Chapter 1

INTRODUCTION

In nature, periodic and symmetric patterns are observed everywhere. For example, the sand waves are almost equally distant from each other and the marks on the skin of felids are remarkably periodic (Fig. 1.1). The examples can be expanded from living creatures (plants, animals, etc.) to inorganic substances (sand, shell, etc.). The subject of this thesis is the periodic and symmetric patterns observed in solidified materials such as cast or welded parts. The production of these types of parts involves melting of metals and controlled cooling of these molten metals into solid parts. By looking at the microstructures of these materials, one can observe the solidification patterns. These patterns vary under different circumstances, which will be explained in following section.

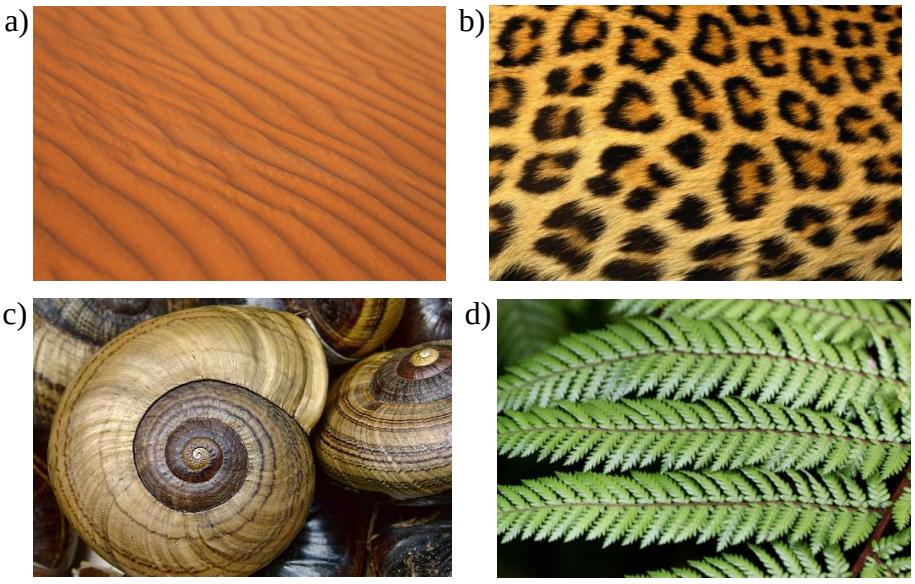

Figure 1.1: Patterns from nature. a) Sand waves, b) Felid skin, c) Seashell, d) Plant.

1.1 Solidification Microstructures

Solidification microstructures are the micro-scale patterns formed upon liquid to solid phase transformation. The solidification patterns and the dynamics leading to those patterns are the interest of scientists and engineers from many fields including physics, metallurgy, and materials science. The understanding of fundamentals regarding solidification patterns is

quite important because mechanical and physical properties of the materials are directly related to the microstructure. In fact, the control of the microstructural features leads to control and optimization of the material properties. There are various types of solidification microstructures depending on parameters like phase diagram of the system, solidification rate, composition, surface energy, and orientation differences between crystalline phases. Solidification microstructures are typically classified into three main groups, namely, dendritic, cellular, and eutectic structures, which are given in Fig. 1.2 as examples. This thesis is about the solidification dynamics of eutectic microstructures.

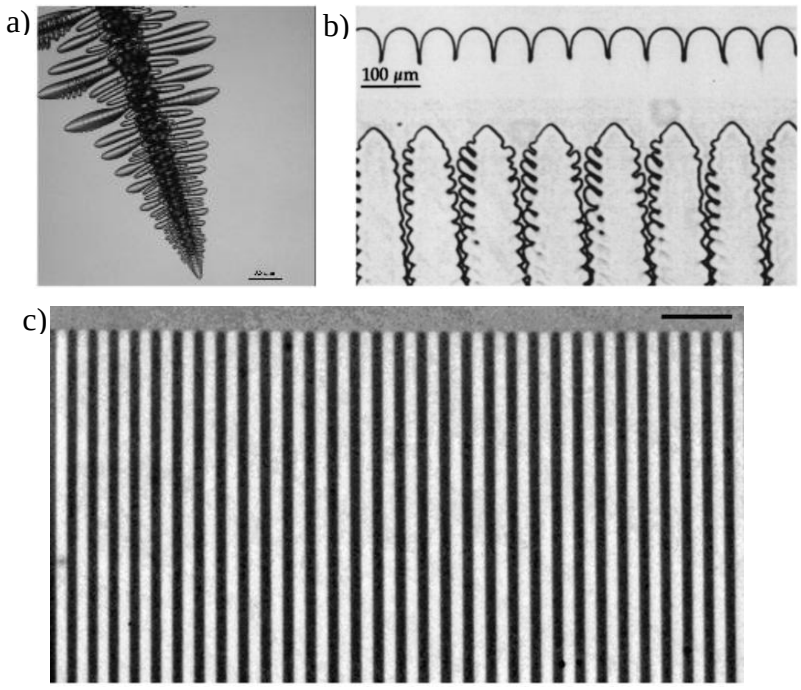

Figure 1.2: a) A micrograph of a pure succinonitrile dendrite. Scale bar shows 500 μm [3]. b) Top: Cell pattern; Bottom: Dendrite pattern [4]. c) Periodic lamellar pattern of In-In_2Bi eutectic. Scale bar shows 50 μm [5].

1.2 Eutectics

Eutectics are the systems forming eutectic microstructures by solidification phase transformation and these structures are observed commonly in many metallic, ceramic, polymeric, and organic systems. In the phase diagram of such a binary system, i.e. an alloy with two components (Fig. 1.3), there is an invariant point called eutectic point at which liquid and two solid phases coexist in equilibrium. Right below the eutectic temperature, eutectic reaction, i.e. transformation of the liquid into two solid phases, $L \rightarrow \alpha + \beta$, takes place. As a result, micro-scale composite structure of α and β phases form upon solidification of a liquid at or near eutectic composition. Due to this composite structure, eutectic materials

have preferable properties. Besides, the eutectic reaction occurs at lower temperatures than the melting temperatures of the components. Due to the ease of melting, production, and preferred properties, eutectic materials, such as cast irons and Al-Si alloys, are used extensively in the industry.

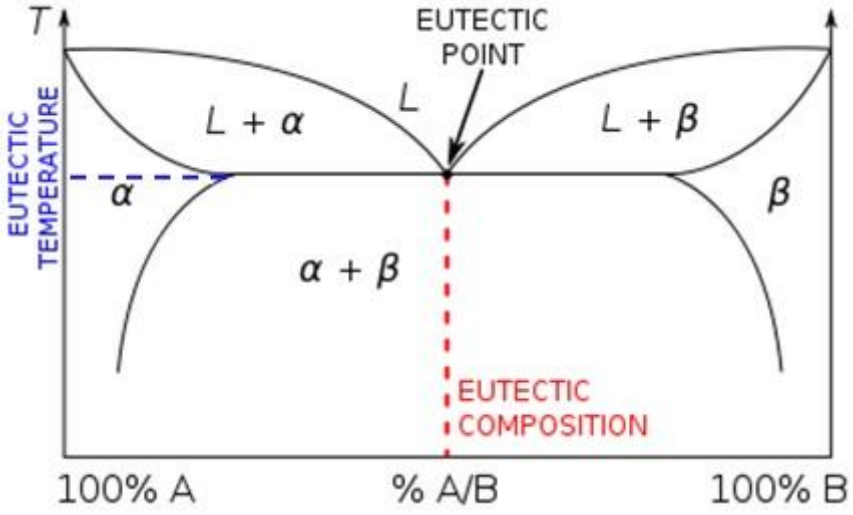

Figure 1.3: Hypothetical binary phase diagram [6].

1.2.1 Two-Phased Eutectics

The majority of the studies in the literature focus on binary eutectic systems with isotropic solid/liquid and solid/solid interface properties due to their simplicity. Two-phased eutectics are formed either in binary systems at or near the eutectic composition or in ternary systems along the univariant composition. In the sections below, literature review regarding binary eutectic systems is given.

1.2.1.1 Eutectic Growth Morphologies

Different eutectic morphologies (Fig. 1.4 and 1.5) may emerge upon solidification depending on the composition of the alloy, phase fraction, solidification rate, solid/liquid, and solid/solid interfacial energies of the phases. In Fig. 1.4, lamellar and rod-like eutectic morphologies are given, which are generally formed as a function of phase fraction of the minority phase. When the phase fractions are comparable to each other, lamellar eutectic forms; whereas major differences in phase fraction result in rod-like morphology. Eutectic composition and the solid solubility of the individual phases determine the phase fraction in local-equilibrium conditions.

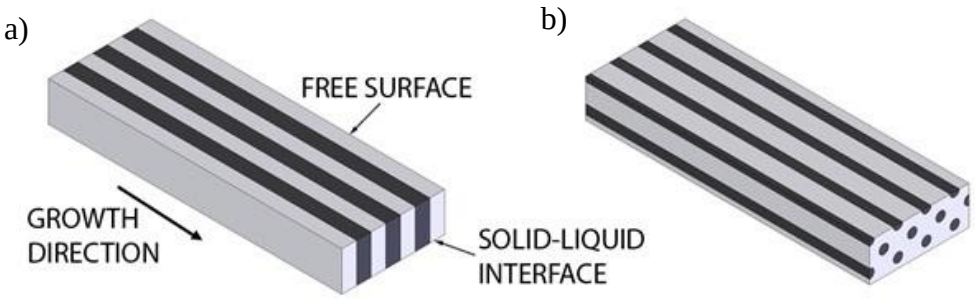

Figure 1.4: Eutectic morphologies classified according to the phase fraction of the minor phase as a) Lamellar eutectic, b) Rod-like eutectic [7].

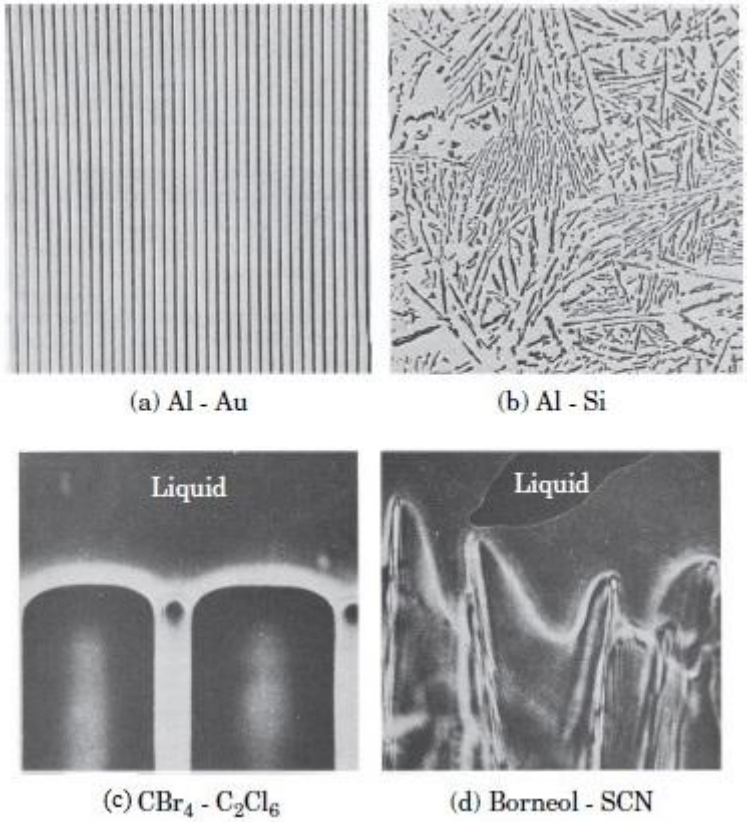

Figure 1.5: Regular and irregular eutectics: a) Regular Al-Au eutectic observed in a longitudinal section; b) Irregular Al-Si eutectic observed in a transverse section; c) Regular CBr_4-C_2Cl_6 eutectic observed in longitudinal view during growth; d) An irregular borneol-succinonitrile eutectic observed in longitudinal view during growth. Images received from Ref. [3].

Additionally, depending on their solid/liquid interfacial energies, eutectic morphologies can be classified as regular and irregular eutectics. In both regular and irregular eutectics, triple junctions, i.e. the intersection of the equilibrium phases α, β, and L, is maintained which enables the coupled growth mechanism. Regular eutectics are observed when both solid phases are non-faceted, i.e. when the entropy of fusion of both phases are low or

solid/liquid interfacial energies are isotropic (Fig. 1.4, Fig. 1.5 (a), and Fig. 1.5 (c)) [2]. When one of the phases is faceted, i.e. the solid/liquid interface is atomistically sharp, irregular type of eutectics form (Fig. 1.5 (b) and Fig. 1.5 (d)). Commonly used industrial alloys of Al-Si and gray cast iron are irregular eutectics where silicon and graphite, respectively, are the faceted phases. Note that microstructures in Fig.1.5 are taken from different sections of the materials. Longitudinal section is a section parallel to the growth direction; whereas, transverse section is perpendicular to the growth direction and parallel to the solid/liquid interface plane.

1.2.1.2 Coupled-Growth Mechanism

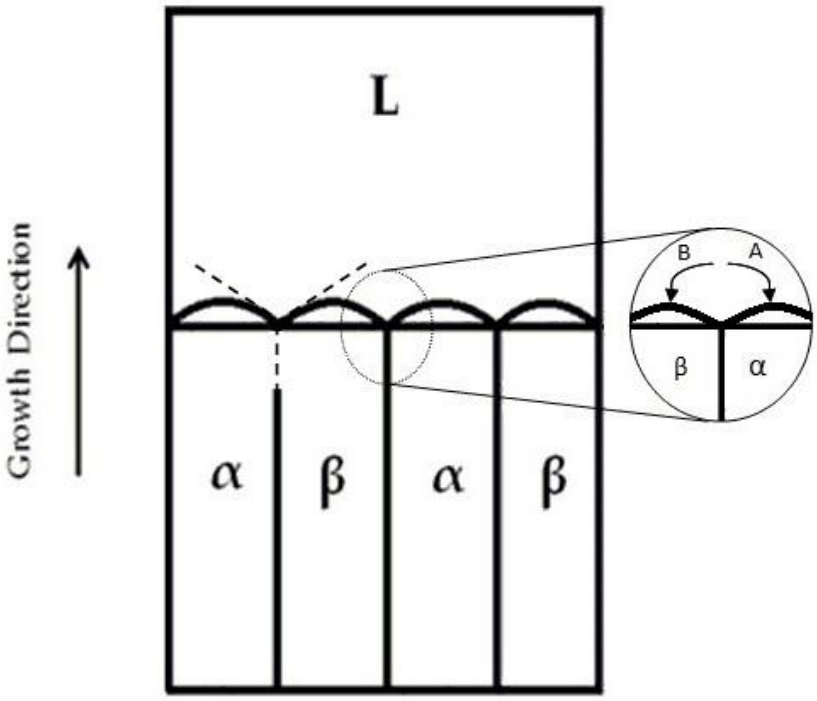

Figure 1.6: Schematic representation of coupled growth mechanism of two-phased system. A and B are the main elements found in α and β phases, respectively. The intersection of the dashed lines shows the triple junction between α, β and L.

Although different morphologies can emerge from a binary eutectic system, the common feature in almost all of them is the coupled-growth mechanism. It is the mechanism which enables growth of α and β phases side-by-side and simultaneously. As seen in the Fig. 1.6, while α phase has to reject B and get A to be able to grow, β phase has to reject A and get B. The growth of two solid phases, α and β, involves the exchange of rejected solutes through liquid right in front of the interface (Fig. 1.6). The coupled growth is kinetically preferred

during growth since it provides a faster and much more efficient mechanism for solute diffusion than the independent growth of each phase by decreasing the diffusion distance compared to single-phase growth [3].

1.2.1.3. Stability of Regular and Isotropic Eutectic Systems

Jackson and Hunt (JH) proposed the most comprehensive theory regarding the solidification of two-phased regular eutectics in 1966 [2]. This theory provides basic explanation for the phenomena involved in the coupled isothermal growth of regular eutectics, which is important to understand JH analysis to be able to examine the results of this thesis. JH formulated the undercooling, ΔT, for regular eutectic steady-state growth as:

$$\Delta T = K_r V \lambda + \frac{K_c}{\lambda} \qquad (1.1)$$

where K_r and K_c are JH constants, V is the growth velocity, and λ is the eutectic spacing, which is the distance between the repeating units of a lamellar pattern. The undercooling has two main components, namely solute and curvature undercoolings. The first term of Eq. (1.1) expresses the contribution of solutal diffusion at the eutectic front due to the coupled-growth mechanism. The second term expresses the contribution of curvature undercooling resulting from the Laplace-Young condition at the triple junction of α, β, and L phases (Fig. 1.6). This equation is plotted in Fig. 1.7 for a hypothetical alloy as ΔT vs. λ at three different growth velocities [3]. The minimum undercooling spacing (λ_m) for these different velocities are shown with the geometric shapes on the curves and capillarity (curvature undercooling) and diffusion branches are shown. As the velocity increases from bottom to middle curve, for example, the minimum undercooling spacing is decreasing from square to circle.

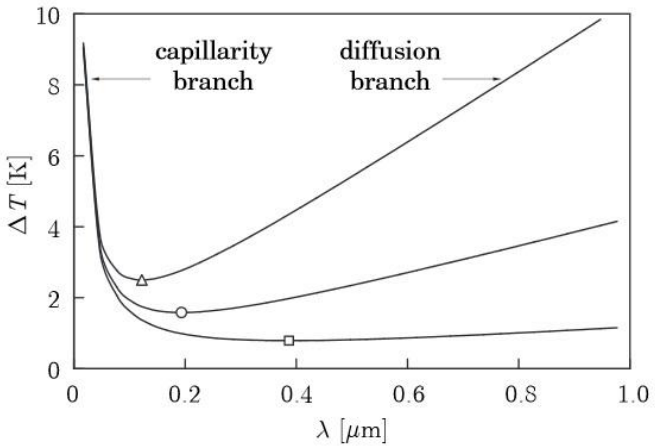

Figure 1.7: Undercooling of the eutectic front, ΔT, as a function of characteristic eutectic spacing, λ, for 3 different growth velocities: V = 100 (bottom curve), 400 (middle curve), and 1000 μms^{-1} (top curve). The symbols indicate the position of the minimum undercooling (λ_m) [3].

Among all the λ values plotted in Fig. 1.7, only a section is stable and hence can be observed experimentally. Outside of this stable range, the microstructure adapts itself to changes in velocity using various eutectic spacing adjustment mechanisms in order to put the system back to the stable range. Experiments conducted by JH using transparent organic CBr_4-C_2Cl_6 eutectic alloy show that when the velocity decreases and λ becomes smaller than the lower limit of the stable range, the system eliminates a lamellar by an overgrowth mechanism in order to adapt itself to the new velocity (Fig. 1.8 (a)). On the other hand, when the velocity increases such that λ becomes larger than the upper limit of the stable range, JH suggested that in order to decrease the spacing, solute builds up ahead of the wider lamella until the lamella of other phase nucleates in the middle (Fig. 1.8 (b)). In fact, the studies conducted years later showed that beyond the upper limit, the wide lamella is branching instead of the nucleation of new a lamella of the other phase [8]. JH also stated that triple-point junctions can only move in the growth direction; however studies later showed that after both the elimination and branching processes, the system changes the eutectic spacing of neighboring lamellae by lateral adjustment, which is called phase diffusion where the differences in eutectic spacing change by the movement of triple-point junction in lateral direction [9]. Finally, JH concluded that the regular eutectics cannot grow below λ_m [3]. In other words, the minimum undercooling spacing value corresponds to the lower limit of stability range for a given velocity. Further experimental and numerical studies, however, showed that the lower limit of stability is lower than the minimum undercooling spacing [8-

10] and at the upper limit; different spacing adjustment mechanisms can be observed [11, 12]. Note that at the point where undercooling is minimum, second derivative of Eq. (1.1) gives;

$$\lambda_m = \lambda_{JH} = \left(\frac{K_c}{K_r V}\right)^{1/2} \quad \text{or} \quad \lambda_{JH}^2 V = \frac{K_c}{K_r} \qquad (1.2)$$

where $\lambda_{JH}^2 V$ is the Jackson and Hunt constant defined as scaling parameter of λ and V.

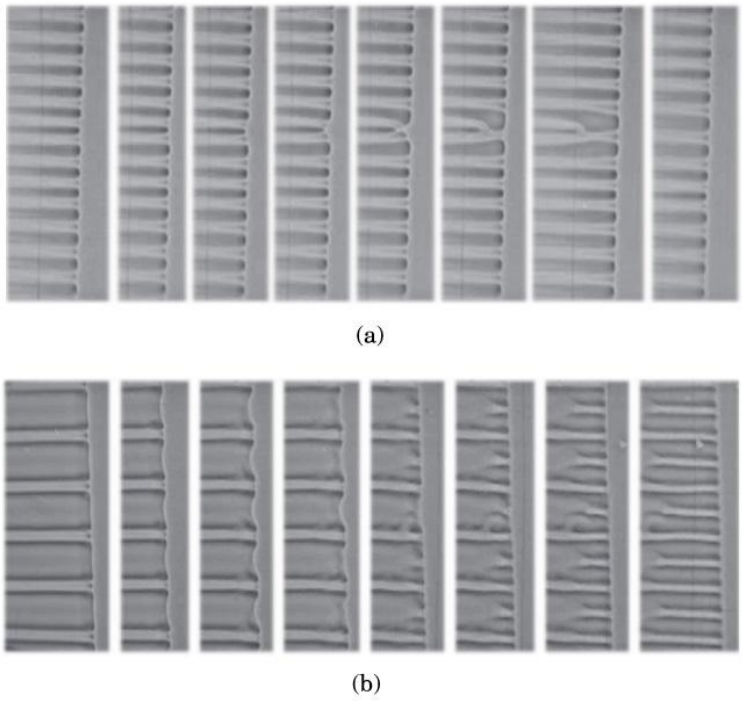

Figure 1.8: Adaptation of lamellar spacing as a result of velocity change in CBr_4-C_2Cl_6 eutectic alloy. a) Decrease in velocity leading to lamellae elimination. b) Increase in velocity leading to creation of lamellae. (Sequences of pictures assembled from the movie of Jackson and Hunt by authors of reference [3]).

In 1980's, the solidification microstructures were classified as out-of-equilibrium patterns by physicists and eutectic solidification was started to be studied using the methods of non-linear physics [11, 12]. Faivre and co-workers established that the regular eutectics can grow at steady-state below the λ_m or λ_{JH} [8, 10]. In other words, the minimum undercooling spacing (λ_{JH}) is not the lowest stable spacing during eutectic growth. After a series of experiments on 12μm-thick (2D) transparent eutectic alloy of CBr_4-C_2Cl_6, they found that the basic state of eutectic microstructure can grow down to $0.7\lambda_{JH}$. Another study carried out by Akamatsu et al. about the eutectic growth in transparent regular eutectic alloy of

succinonitrile-(D)camphor (SCN-DC), revealed that the lower stability limit can be as small as $0.65\lambda_{JH}$ [13]. By not only using transparent alloys, but also using the metallic alloys, the lower limit is proved to be lower than λ_{JH}. For example, as a result of thin-sample directional solidification of In-In_2Bi metallic eutectic alloy, the stability of spacing is found to be extending from about $0.9\lambda_{JH}$ to $2.2\lambda_{JH}$ [5]. Hence, the fact that minimum undercooling spacing is not the lowest stable spacing during eutectic growth is well established. On the other hand, along the diffusion branch, oscillatory modes, namely 1λO and 2λO, were observed after an upper critical spacing value [8, 10, 14]. It is called 2λ oscillations because the pattern repeats itself in every 2λ (Fig. 1.9).

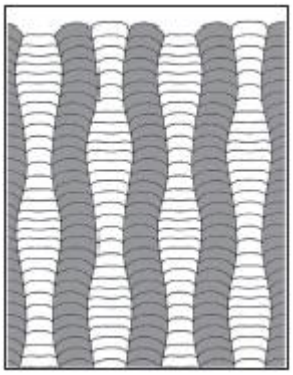

Figure 1.9: 2λ oscillations. Image is taken from Ref. [3].

1.2.2. Three-Phased Eutectics

In ternary eutectic systems, the microstructure formed upon solidification of the liquid phase at the invariant composition into three solid phases simultaneously is called three-phased eutectics. Also, they can be observed along the univariant of quaternary - four components - systems. The introduction of a third element into a binary eutectic system and forming ternary eutectic point results in a decrease of the melting temperature, providing more fusible and easier to process materials. However, the presence of a third phase increases the complexity of the pattern selection problem substantially due to the countless number of possibilities for microstructural arrangement. In other words, while binary eutectics can be arranged only in ABABABAB order, three phased eutectics can be arranged in ABAC, ABC, ABABABACACAC, etc. orders.

Three-phased eutectics have been studied for just over a decade, and the stability of different patterns, their stability limits, and the spacing adjustment mechanisms are still unknown both for 2D and 3D samples. The studies performed so far mostly examined the

ternary phase diagrams or reported the three-phased microstructures observed without examining their stability [15-35]. ABAC type pattern has been observed in 2D samples by Boettinger and Witusiewicz et al. using Pb-Sn-Cd and In-Bi-Sn alloys, respectively [34, 35]. Moreover, in the literature, there are two $\lambda^2 V$ constants found by Ruggiero et al. and Witusiewicz et al. for three-phased eutectic patterns of In-Bi-Sn system [35, 36]. These constants are calculated by applying $\lambda^2 V$ fit to the measured eutectic spacing data points taken from the images of stable ABAC patterns. However, due to its definition, it is more significant and conclusive to calculate $\lambda^2 V$ constant using minimum undercooling spacing $\lambda_m(\lambda_{JH})$ instead of using any stable eutectic spacing λ.

In 3D samples, the morphological studies on cross-sectional view of Al-Ag-Cu ternary eutectic showed ribbon-like eutectic structure where B and C phases form the ribbon and A phase forms the matrix (Fig. 1.10) [37].

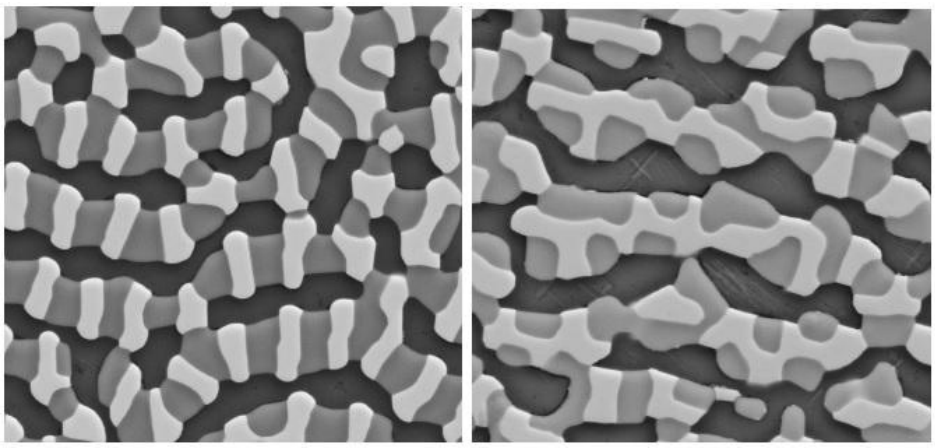

Figure 1.10: Ribbon-like microstructures found in three-phased eutectic of Al-Cu-Ag system. The images are taken from two different grains of the same transverse cross-section solidified at 4.0 μm/s. The white phase is Ag_2Al, the light gray phase is Al_2Cu, and the dark gray phase is α(Al) [37].

2D phase-field models, which are used to simulate the solidification dynamics, predicted the microstructural arrangements in three-phased lamellar eutectics as well. For instance, Choudhury et al. reported that the possible stable arrangements of phases are in ABAC and ABC orders [1]. They also presented some results regarding the stability of these orders. In fact, they simulated the behaviors of ABAC and ABC type of eutectic patterns at low spacing and large spacing values. At low spacings, they found that ABAC pattern evolves to the ABC arrangement by eliminating one of the A lamella both at eutectic and off-eutectic

concentrations. In fact, since they used only one motif of ABAC in the simulations, there are no other chances other than turning into an ABC pattern upon elimination. Also, due to the same reason, they cannot provide information about diffusion of eutectic spacing in the simulations. At large spacings, these patterns experienced various oscillatory modes at different concentrations (Fig. 1.11).

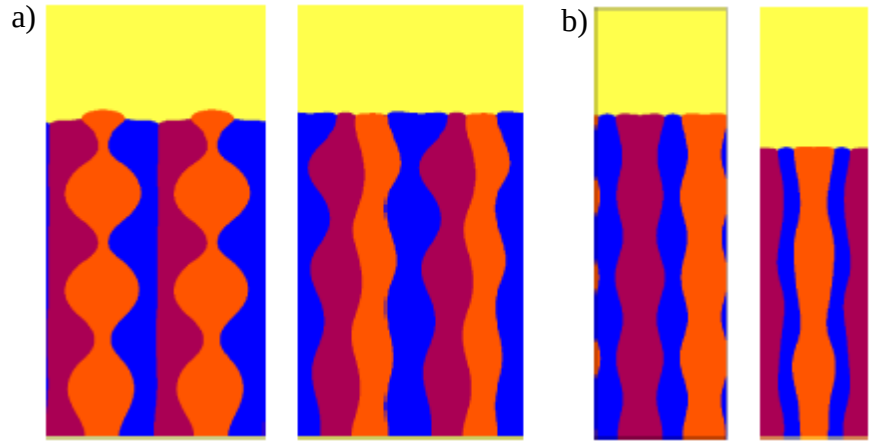

Figure 1.11: Simulations of oscillatory modes of the a) ABC and b) ABAC patterns. Left image in b) is at eutectic concentration and concentrations are off-eutectic for other simulations. Images are taken from Ref. [1].

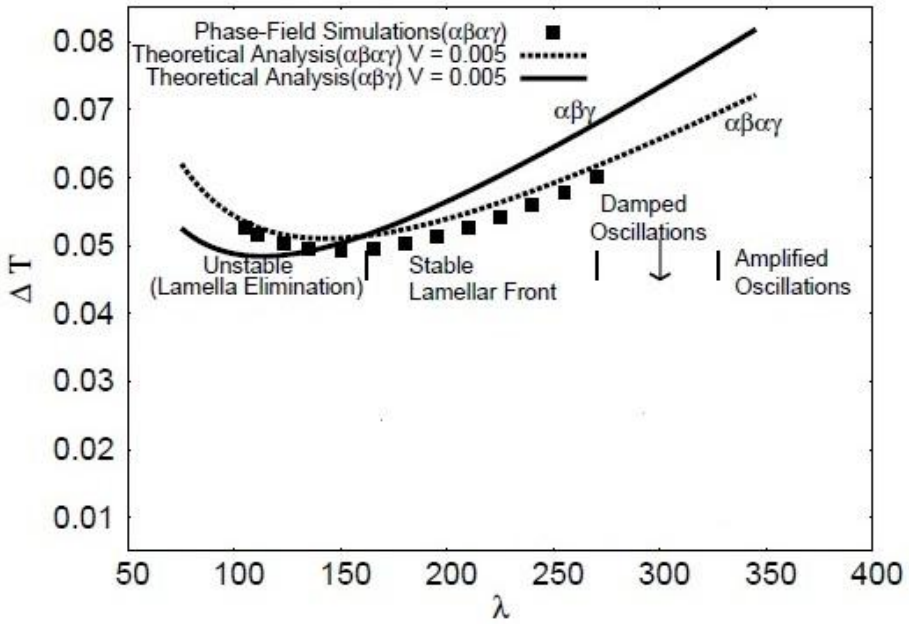

Figure 1.12: Comparison between ABC and ABAC patterns with respect to theoretical and numerical analyses. Image is taken from Ref. [1].

Also, theoretical and numerical analyses of ABC and ABAC arrangements as a function of ΔT and λ are shown in Fig. 1.12. Simulations results show the ABAC to ABC evolution below the lower limit of spacing (left side of the curves) and the oscillatory behavior at large spacing values (right side of the curves). If the eutectic spacing value is close to the stable eutectic growth range, oscillations are damped, but if it is above a critical value, oscillations are amplified.

Dynamic stability of three-phased patterns during thin-sample directional solidification of a ternary eutectic alloy is the main subject of this thesis. It aims to find the answers to the following arising questions: *(i)* What are the possible stable microstructures in three-phased eutectics in 2D samples? *(ii)* How does the system reacts to the growth velocity changes? *(iii)* What are the stability limits of a three-phased microstructure? *(iv)* What happens beyond these limits? *(v)* What are the spacing adjustment mechanisms? *(vi)* What are the JH and phase diffusion constants for a given system? In this thesis, In-Bi-Sn isotropic ternary eutectic system was used and directional solidification experiments of thin specimens were conducted in order to understand the periodic steady-state microstructures, as well as the stability of these microstructures. This alloy system is in the class of lead-free solders, which are commonly used to get rid of the toxic behavior of lead to the human life and environment [38], to join the electronic parts mechanically or electrically.

Chapter 2

EXPERIMENTAL PROCEDURE

In the course of this thesis, which involves the investigation of solidification dynamics of three-phased eutectic growth for isotropic systems, directional solidification (DS) method is used where sample is pushed at a fixed velocity, *V*, towards the cold side of the unidirectional thermal gradient, *G*. In-Bi-Sn system is chosen for this study due to having low eutectic temperature, T_E, isotropic solid/liquid interfaces, and well-established phase diagram. Having low T_E is extremely critical to enable real-time investigation using an optical microscope, since the temperature gradient stage has to be placed very close to optics of the microscope. The experiments are conducted using 2D specimens to simplify the already existing complexity of the three-phased structures by decreasing the variations in the microstructural features of the eutectic pattern throughout the thickness of the specimen. In the following sections, the detailed information regarding the alloy and sample preparation, solidification set-up and procedure followed in experiments are image analyses are given.

2.1. Alloy Preparation

There are two ternary eutectic points in In-Bi-Sn system as seen in the phase diagram (Fig. 2.1). Due to having lower T_E and isotropic S/L interfacial energies of the phases, the ternary eutectic system marked as E_2 on the phase diagram is chosen for this study. For this three-phased system, T_E = 59.2 ^oC and C_E = In51.2 - Bi32.0 - Sn16.8 wt% and the corresponding eutectic phases are β-In, In_2Bi and γ-Sn [39].

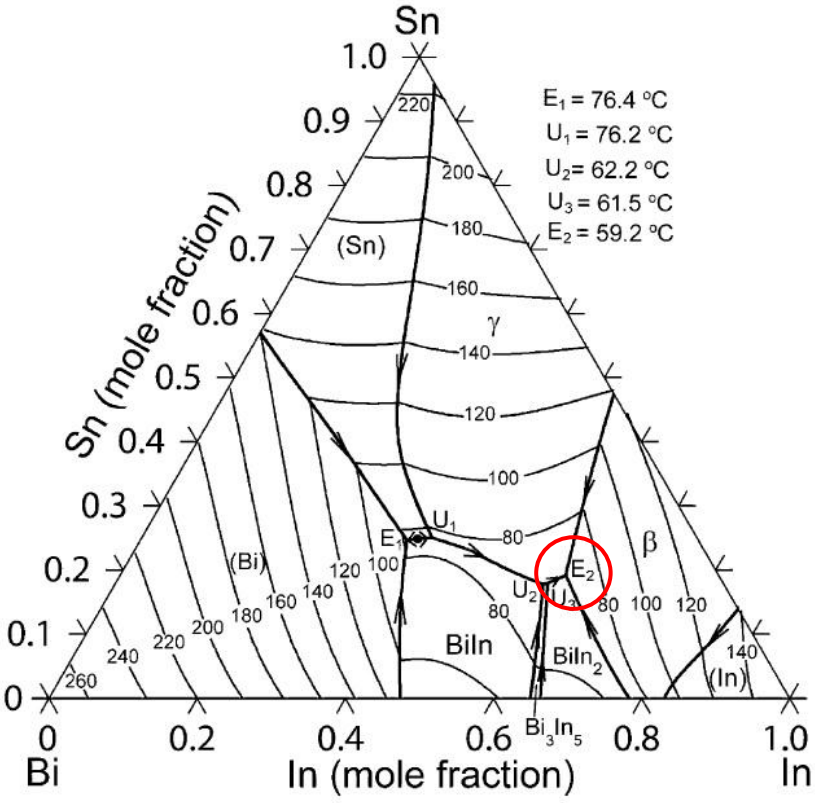

Figure 2.1: Phase diagram of In-Bi-Sn system. Isotherms are given in ^{o}C [39]. Chosen eutectic system is marked with circle.

The eutectic alloy is prepared using 99.999% pure indium, bismuth and tin elements (Goodfellow). Oxide layer is observed on Bi particles and the layer is removed by washing it in concentrated HCl for 2-3 mins. Then, the particles are immersed in the pure water and dried in an oven at 78 ^{o}C for about 2 mins. Necessary amounts of metals are calculated according to In amount and measured using a balance with 10^{-4} grams precision. The alloy is melted and mixed under a vacuum atmosphere (10^{-2} mbar) using a hot plate/stirrer.

2.2. Sample Preparation and Filling

The sample containers are prepared using two thin (≈ 300 μm) borosilicate glass plates and placing thin (12 μm-thick) mylar spacers in between (Fig. 2.2 (a)). The glass plates provide the transparency required for real-time analysis using optical microscope. In this study, 12 μm-thick high temperature resistant mylar spacers were used in order to obtain 2D specimens. Glass plates are glued together with NOA81 adhesive material, which is also high temperature resistant and can be polymerized quickly with UV light exposure. One side of the sample is left open i.e. without glue, to be able to fill the molten alloy in between glass plates using pressure filling.

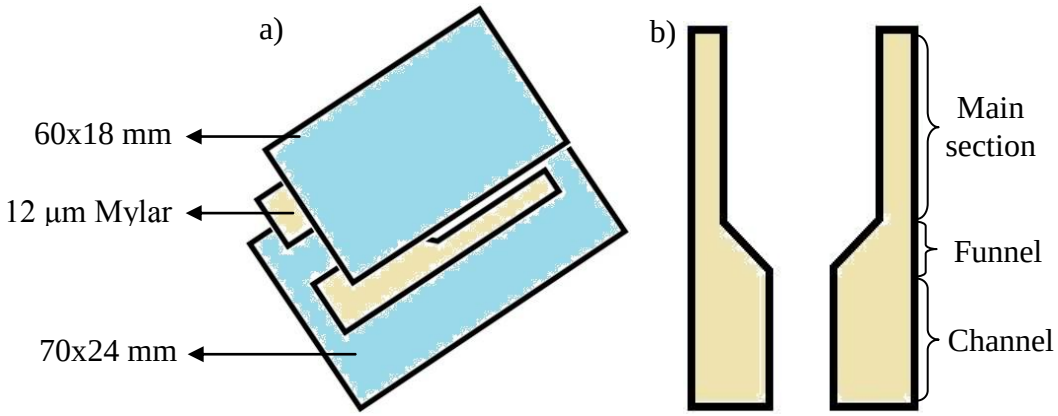

Figure 2.2: Schematic representation of a) the sample showing glass plates and the mylar spacers, and b) mylar cut showing the sections.

The shape of sample is set by cutting the mylar spacers in a desired shape as shown in Fig. 2.2 (b). It consists of a narrow channel where solidification starts and grain selection process takes place. When the selected grain reaches the funnel, it invades towards the side of the sample and eventually at the main section, a large-enough grain is obtained for analysis. In fact, the narrow channel is used to obtain a single grain, which eliminates the complexity of a three-phased system by decreasing the possibility of different grain formations.

The cleaning procedures of glass plates are highly critical due to affecting the purity and hence the microstructural features of the alloy as well as creating defects which influence the solidification dynamics. Before the start of the cleaning procedure, the glass plates' thicknesses are measured and recorded. Then, plates are put in sulfuric acid (H_2SO_4) and washed with pure water. Next, they are cleaned in a glass cup filled with pure acetone within an ultrasonic cleaning machine for 15 min. After changing acetone with pure water and Hellmanex™ mixture, they are cleaned again in an ultrasonic cleaning machine for 15 min. at 30 ^{o}C. Hellmanex™ is an alkaline liquid concentrate, which significantly reduces the surface tension of water resulting in good wetting and hence cleaning. Finally, ultrasound machine is turned off and waited for almost 2 hours to let unwanted particles sink before they are washed with ultra-pure water.

Once empty sample containers are ready, they are filled with the alloy following the procedure explained below. First, the alloy bottle is placed inside the large glass container (Fig. 2.3) and the empty sample is attached to a glass rod inside the glass container. After making sure the whole set-up including cold trap, vacuum manifold, and glass container is tightly sealed, the container is vacuumed to 10^{-2} mbar and pressurized with Ar. The process is

repeated 3 times to minimize the oxygen left inside the container. Note that a vacuum trap with liquid nitrogen inside a dewar is used to avoid any unwanted particles reaching to pump or atmosphere during vacuum. After reaching 10^{-2} mbar vacuum, the glass container is heated up using the hot plate/stirrer to melt the alloy. The heater is set to 100 – 120 ^{o}C and heat guns are used externally to preheat the sample container to let the alloy melt move inside the crucible, since heating with convection is difficult without air. When the melt is ready, the empty sample is inserted inside the alloy. Unless the alloy fills the sample by capillarity, pressurized Argon around 1 atm is send to the container to push the molten alloy upwards inside the sample (Fig. 2.4). The alloy is cooled fast to avoid any microsegregation. Finally, the open end of the sample is sealed with NOA81 at room temperature and fixed to holders to be inserted in the directional solidification set-up.

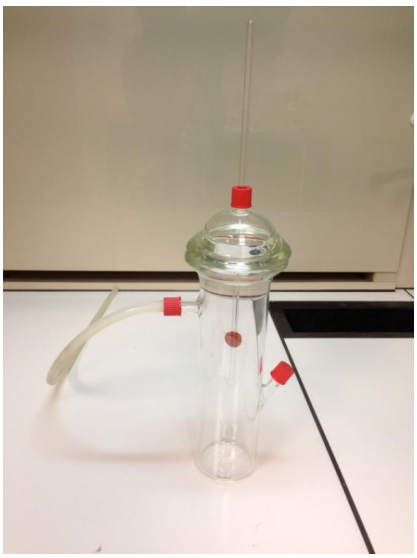

Figure 2.3: The glass container used for sample filling.

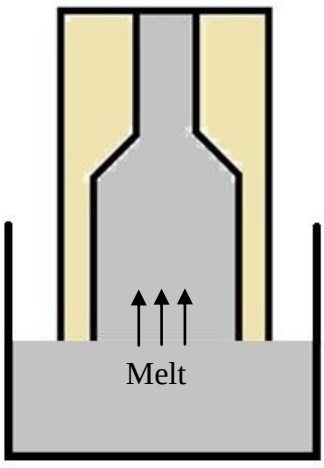

Figure 2.4: Filling the empty sample with the molten alloy.

2.3. Experimental Set-up

The directional solidification (DS) set-up (Fig. 2.5) includes heating and cooling systems to establish unidirectional thermal gradient, and a motion control system to move the sample along this thermal gradient for solidification. The whole set-up is fixed on a microscope stage for in-situ investigation and analysis.

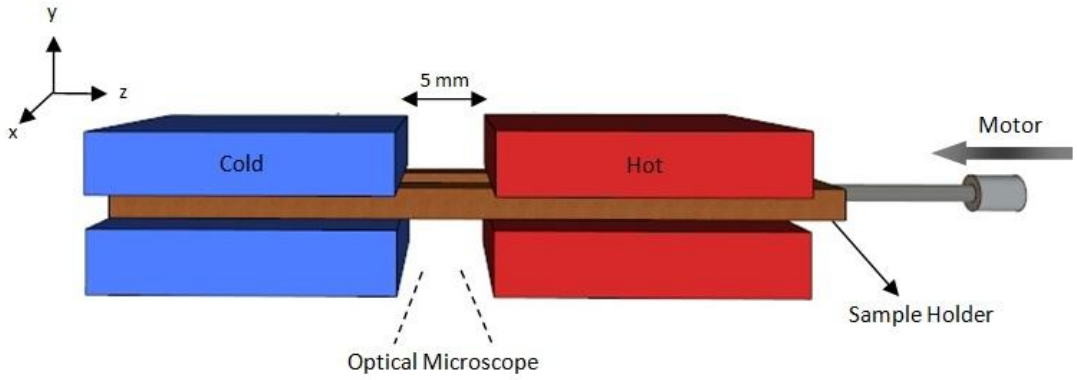

Figure 2.5: Schematic representation of the experimental setup.

The schematic representation of DS set-up used in the experiments is given in Fig. 2.5. The sample is sandwiched between copper blocks, which are used due to the high thermal conductivity of copper. Cooling is achieved by water circulation inside the cold blocks, while the resistance heaters inside the hot blocks are heated by applied voltage for the hot part. Cold and hot blocks are set to 20 ^{o}C and 80 ^{o}C, respectively. The gap between the blocks is fixed to 5 mm and can be changed to adjust the temperature gradient. In order to measure the thermal gradient, thermocouples are attached to the empty sample moving in between the copper blocks and temperature change with respect the position is measured using a temperature reader and recording the time. With 5 mm distance between the blocks, the thermal gradient at the solidification front is measured as 8 ± 0.9 K/mm. A high-resolution motor with 50 mm travel range is attached to the sample holder to move the sample along the unidirectional temperature gradient. In Fig. 2.5, x is the axis parallel to the growth front, y is the axis perpendicular to the sample plane and z is the thermal gradient axis. This set-up is fixed on the stage of optical microscope and the solidification front is observed from the lower glass plate of the container through the gap using reflection microscopy. The microstructures are observed with 10x magnification and the images are recorded with a monochrome digital camera to a computer for further processing and analysis. The reflectivity variation between different types of glass/phase surfaces give rise to a contrast

resulting in white appearance of β-In, black appearance of In_2Bi and gray appearance of γ-Sn phases (Fig. 2.6) [5].

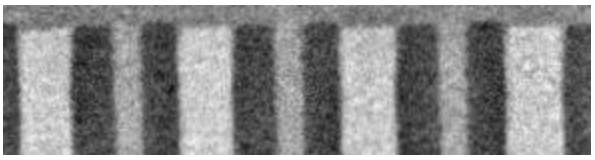

Figure 2.6: The reflectivity difference between eutectic phases. β-In: white, In_2Bi: black, and γ-Sn: gray. Image width: 165 μm.

After setting hot and cold block temperatures and hence thermal gradient, the input parameter of an experiment is the growth velocity, *V*, while the eutectic spacing, *λ*, microstructural and morphological features are the output parameters.

2.4. Initial Procedure for Solidification

An experimental procedure involving several steps are employed in order to obtain isotropic, stable, and periodical pattern in a large-enough grain that can be investigated throughout the experiment. First, the alloy is melted until the solid/liquid interface is in the channel of the sample. Then, the solidification is started at a high velocity (≈ 1 μm/s). Once two-phased (black and gray) isotropic lamellar structure appears (Fig. 2.7), the velocity is decreased gradually to ≈ 0.55 μm/s and waited for the third phase to appear and invade through the solidification front (Fig. 2.8). It is important to wait further without changing the velocity to let the three-phased structure stabilize and for the proper isotropic structure to spread through the funnel part of the sample. Even after the establishment of stable pattern, high velocity differences (≈ 0.15 μm/s) should be avoided, otherwise the disappearance of the white phase would be inevitable.

Throughout the experiments, steady-state patterns are investigated at various growth velocities. Afterwards, in order to examine the limits of stability, the growth velocity has been gradually changed to push the pattern beyond these limits where some spacing adjustment mechanisms are used by the system. In other words, since the material is stable only within a range of eutectic spacing, when it is forced to go beyond the stability range, it is expected to show use spacing adjustment mechanisms to go back to the stable growth pattern. The eutectic spacing values beyond which these mechanisms are observed marks the limits of stability of a given pattern.

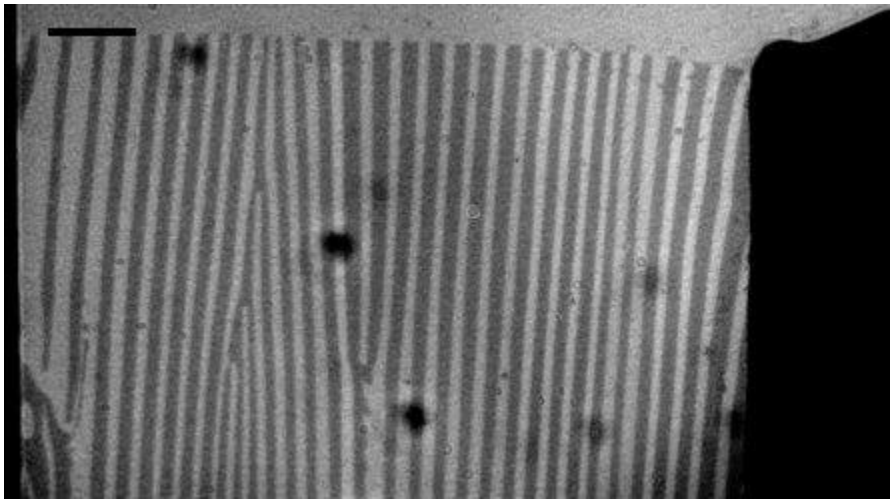

Figure 2.7: Coupled-growth of two phases at the beginning of solidification. Scale: 50 μm.

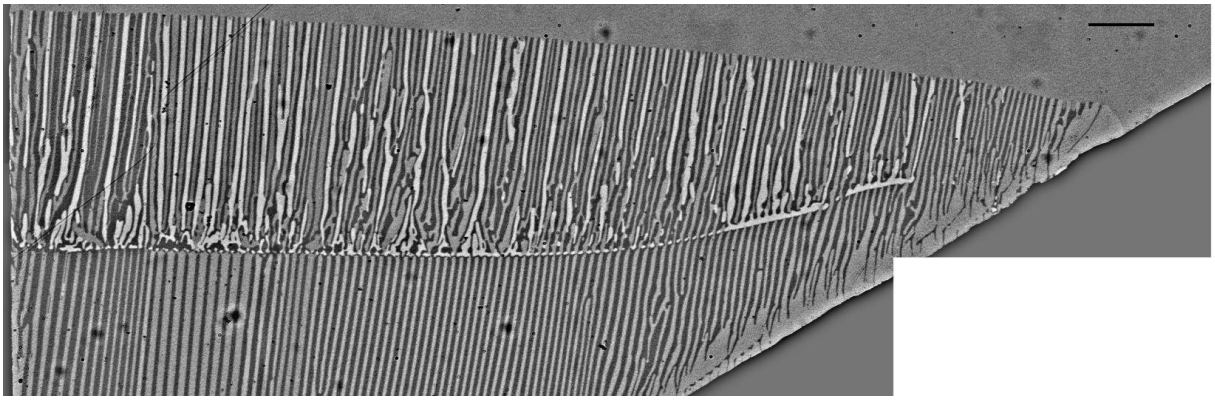

Figure 2.8: Appearance of the third phase. Image is produced by merging 7 images. Scale: 100 μm.

2.5. Image Processing and Analysis

Several image-processing steps are employed to enhance the visualization of phases using ImageJ software. An example of the image processing procedure sequence is given below with the corresponding images with 374 μm width.

- Adjusting Contrast & Brightness

  It is necessary to adjust the contrast and brightness to distinguish the three phases clearly.

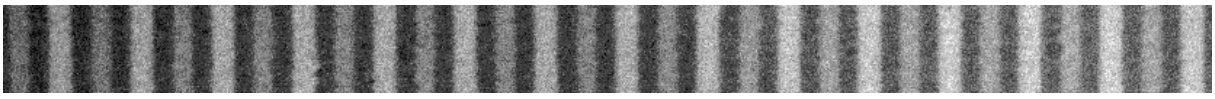

- Extract Background

  A plug-in is used to homogenize the linear light intensity differences in an image due to, for example, shadows of copper blocks.

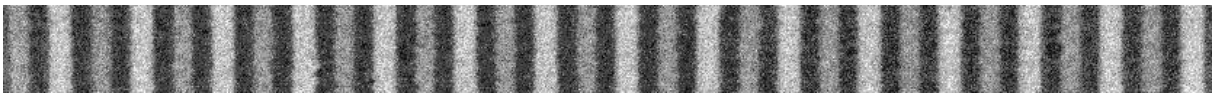

- Smooth

  This function blurs the image, replacing each pixel with the average of its 3x3 neighborhood. It is applied to smooth the sharp edges.

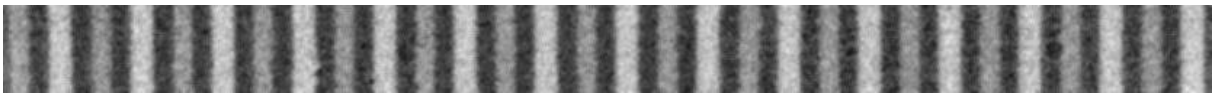

- Despeckle Noise

  It is used to remove the noise resulting from random variation in brightness or color information in images.

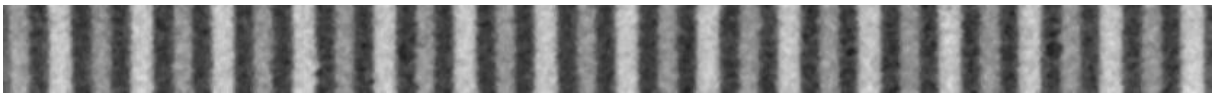

- Threshold

  This procedure is required to obtain binarized image of three-phased structure. The intensity threshold values are adjusted such that black color shows the black phase while the gray and white phases are represented by white color.

- Find Edges

  This procedure finds the edges of black phases.

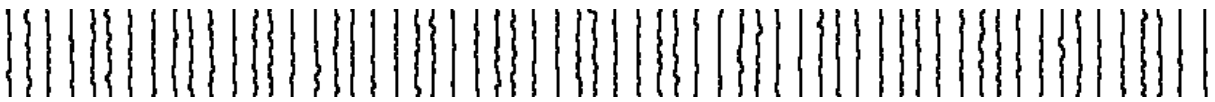

- Analyze Particles

  It is used to calculate the x-axis positions of the edges from their center of mass. In this way, the thickness of each phase as well as the eutectic spacing can be measured.

After the image processing with ImageJ, Kalediagraph is used for graphing and data analysis. The eutectic spacing, λ, is calculated from the difference between edge positions and plotted with respect to x-axis position.

Chapter 3

RESULTS & DISCUSSION

Directional solidification experiments are conducted in order to find the stable three-phased eutectic pattern and the stability limits of it. To find the stable three-phased eutectic pattern, long-lasting experiments at various velocities are performed and the microstructural evolution of the pattern is examined to identify where it is converging. After the establishment of the stable periodic basic state, stability limits of this pattern are investigated. To find the limits, first it is waited until the system reached steady-state at a fixed growth velocity, and afterwards, the growth velocity of the system is changed in order to push the microstructure out of its stability limits. Experiments performed and spacing adjustment mechanisms observed throughout these experiments are summarized in Table 3.1.

In the sections below, first the stable pattern in 2D three-phased eutectic systems is given. Afterwards, observations and measurements regarding the spacing adjustment mechanisms, which are used by the system beyond the stability limits to go back to the stable region, are presented. In the following section, the calculation of phase diffusion coefficient and JH constants using eutectic spacing distribution of growth patterns along the x-axis are given. Finally, some interesting microstructural observations came across throughout the experiments are reported.

3.1. Stable Pattern

In 2D directional solidification of In-Bi-Sn non-variant eutectic alloy, steady-state arrangement of the three phases is found to be in ABAC order, where A, B, and C are In_2Bi, β-In and γ-Sn phases, respectively (Fig. 3.1). The alloy is observed through the glass wall of the container by reflection optical microscopy. The contact surfaces of A, B and C phases with glass have different reflectivity properties by nature, due to which In_2Bi phase appears black, β-In phase appears white and γ-Sn phase appears gray, after contrast and brightness enhancement. Phases were identified based on the chemical compositions of the phases measured by SEM-EDX [35].

Table 3.1: Spacing adjustment mechanisms observed throughout the experiments upon velocity change from V_0 to V_1.

V_0(μm/s)	V_1(μm/s)	Elimination	Oscillation	Branching	Tilt
0.354	0.265	✓			✓
0.283	0.248	✓			✓
0.283	0.071	✓			
0.265	0.212	✓			
0.248	0.219	✓			✓
0.223	0.248		✓	✓	✓
0.212	0.152	✓			
0.205	0.223		✓	✓	✓
0.195	0.124	✓			✓
0.195	0.142	✓			✓
0.188	0.205		✓		✓
0.170	0.188		✓		✓
0.163	0.198		✓	✓	
0.152	0.103		✓		
0.142	0.148		✓	✓	
0.142	0.163		✓		
0.135	0.142		✓		
0.131	0.166		✓	✓	✓
0.113	0.120		✓	✓	
0.106	0.131		✓	✓	
0.106	0.113		✓		
0.103	0.067	✓			
0.099	0.103		✓	✓	
0.092	0.099		✓	✓	
0.089	0.106		✓		
0.085	0.092		✓		
0.071	0.035	✓			✓
0.071	0.043	✓			
0.067	0.046	✓			
0.046	0.024	✓			

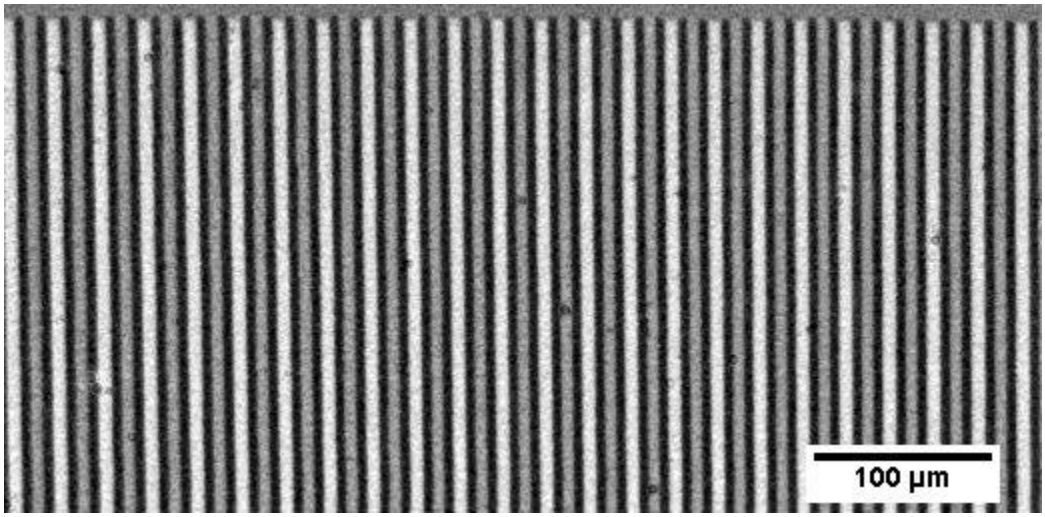

Figure 3.1: The stable ABAC-order lamellar structure of In-Bi-Sn non-variant eutectic alloy directionally grown at V = 0.35 µm/s. Solidification direction is upwards. In_2Bi phase is black, β-In phase is white and γ-Sn phase is gray.

There exist many proofs showing that the stable arrangement is ABAC. After long solidification runs at a constant velocity, the system eliminates all the arrangement faults and forms ABAC pattern. Once ABAC pattern forms, it does not turn into any other arrangement even after long solidification runs, unless the growth velocity is changed; i.e. the stable eutectic spacing range is altered. In that case, the system use various spacing adjustment mechanisms to be stable back again. During elimination spacing adjustment mechanism, not only one-phase is eliminated as in the case of binary eutectics, but all the pattern, i.e. A, B, A, and C phases are eliminated with time to form back the stable ABAC pattern (Fig. 3.2). During branching spacing adjustment mechanism in 2D samples, the ABAC pattern is not obtained back again probably due to branching being a 3D mechanism. Preliminary studies in thicker samples showed that the ABAC pattern is rather easily obtained back after continuous branching of phases. Detailed explanation about spacing adjustment mechanisms will be given in the next section. Moreover, even in tilted morphology, where phases grow with an angle with respect to the direction of thermal gradient, and in asymmetric morphology, where the thickness of In_2Bi phases, i.e. A phase in ABAC pattern, are not the same, ABAC order is observed as the steady-state pattern (Fig. 3.3). Since the stable periodic arrangement obtained in 2D three-phased eutectic systems is ABAC order of phases, the eutectic spacing, i.e. lambda (λ) is defined here as the width of an ABAC pattern.

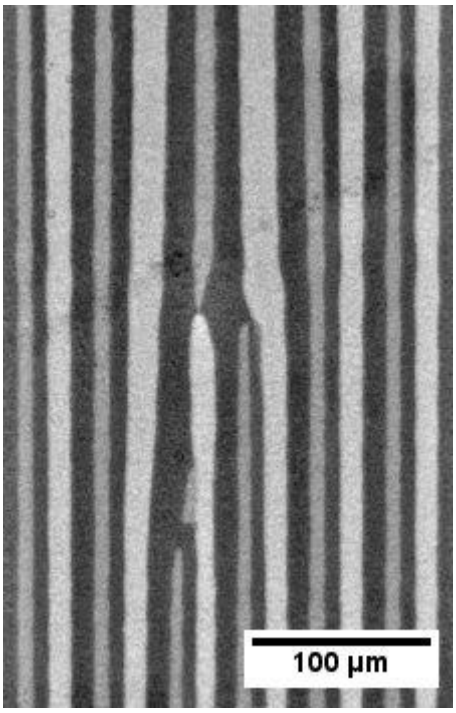

Figure 3.2: Elimination instability of a whole ABAC pattern observed when velocity is dropped from 0.067 µm/s to 0.046 µm/s. Growth direction is upwards. G = 8 K/mm.

In some experiments, tilted ABAC pattern, i.e. ABAC pattern growing with an angle with respect to the thermal gradient axis (Fig. 3.4) is observed. These types of patterns were observed in two-phased eutectics as well. In the literature, one cause of these tilted patterns is reported as the strong interfacial anisotropy of the crystal/crystal interphase, i.e. solid/solid boundary, at which case the microstructure is called as a locked grain [40]. However, the tilted pattern observed in the experiments differs from the ones observed in locked grains since the angle of tilt is not locked to a direction but changes as the growth velocity is altered. Tilt angle measurement as a function of velocity made from two different experiments that are shown in Fig. 3.5 confirms that the angle is not locked to a direction.

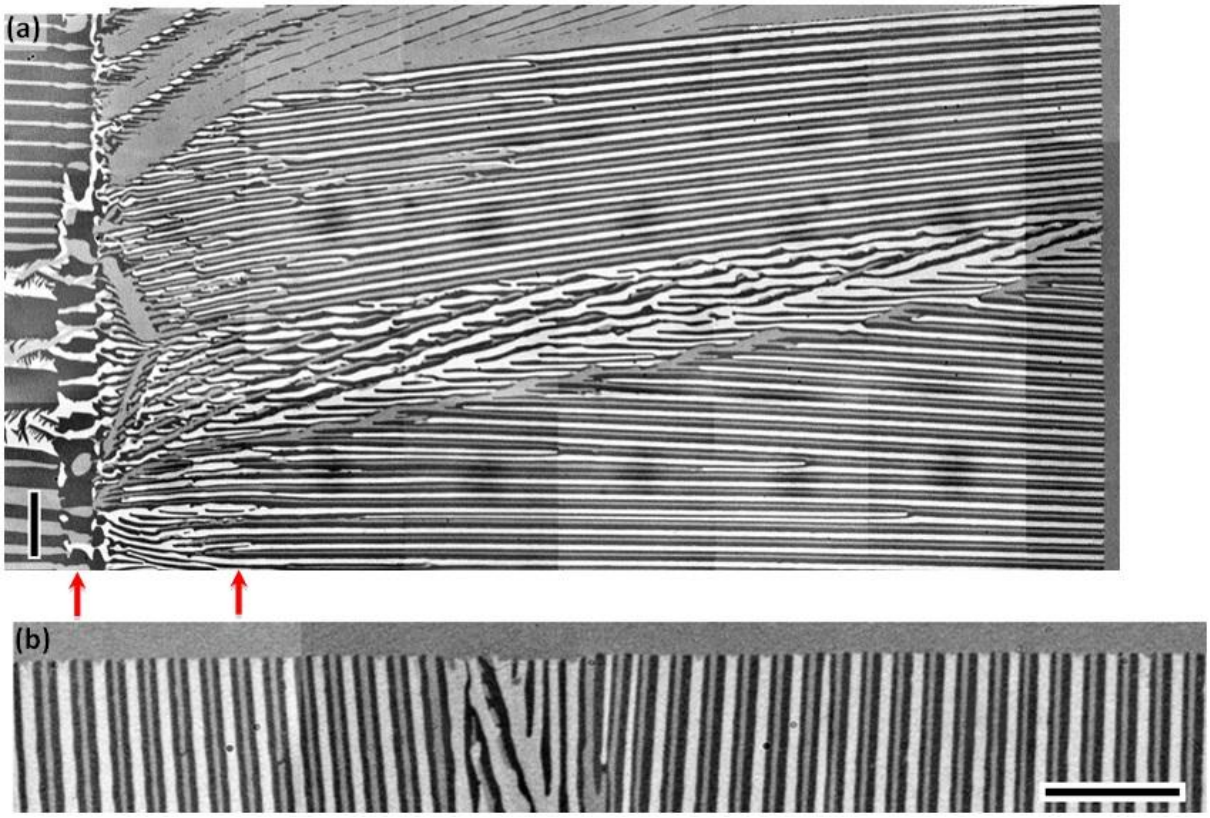

Figure 3.3: ABAC pattern observed in tilted and asymmetric morphologies. a) The formation of ABAC pattern upon solidification of phases in different types of grains. Solidification direction is towards right. The left and right arrow marks indicate where velocity values have been changed. Left arrow: from 0.035 μm/s to 0.708 μm/s and, Right arrow: from 0.708 μm/s to 0.354 μm/s. b) Solid/Liquid interface of the same microstructure. Tilted morphology and asymmetric morphology of In_2Bi phases are observed clearly in left and right grains, respectively. Solidification direction is upwards. Scale bars: 100 μm. G = 8 K/mm.

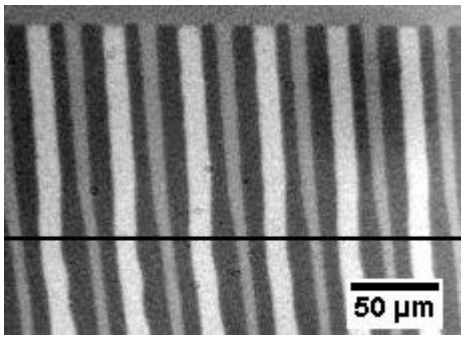

Figure 3.4: Tilted ABAC pattern, i.e. the direction of solid/solid interface is not perpendicular to the solid/liquid interface. Velocity has been changed from 0.25 μm/s to 0.12 μm/s when the solid/liquid interface was at the horizontal line, as a result of which the tilt angle changed from 6 to 4 degrees and the pattern became asymmetric.

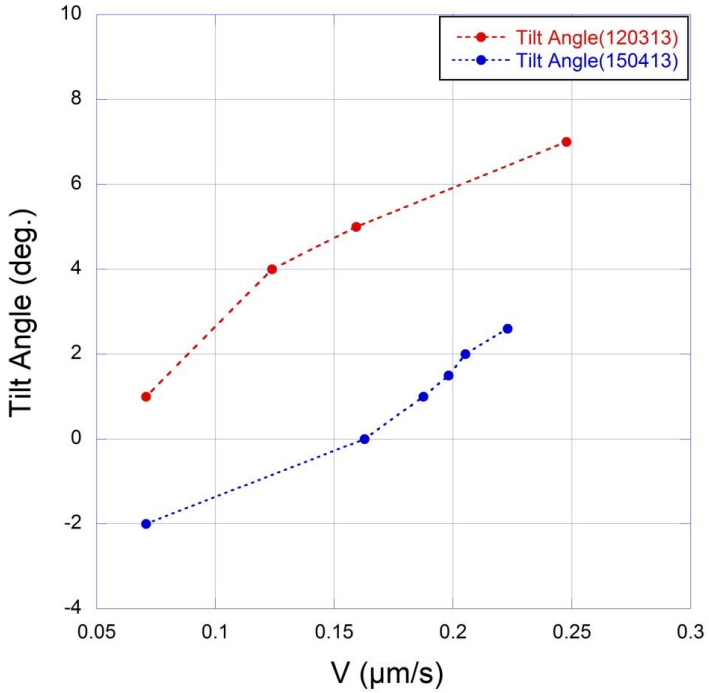

Figure 3.5: Change in the tilt angle as a result of a change in solidification velocity. The data are taken from two different experiments. 0 tilt angle indicates that the crystal/crystal interphase is parallel to the thermal gradient axis.

3.2. Limits of Stability and Spacing Adjustment Mechanisms

After a large enough grain with stable ABAC arrangement is obtained for statistical measurements and to avoid perturbations due to the faults, grain boundaries or edges of the sample, the growth velocity is altered to check the stability of the pattern. Spacing adjustment mechanisms like elimination, oscillation, and branching are observed at the stability thresholds. In order to check the lower limit of stability of the system, the growth velocity is decreased. When the eutectic spacing is smaller than the lower limit of stability, system eliminates a complete pattern of ABAC to be stable back again. Elimination of one ABAC pattern is shown in Fig. 3.6 (a) where dashed lines represent the sections from which eutectic spacing measurements are taken. In Fig. 3.6 (b), the corresponding eutectic spacing (λ) distribution before and after the elimination is plotted. Fig. 3.6 (b) shows that the ABAC spacing value reaches a minimum just before the elimination (meas. 2) right at the location where elimination takes place. This minimum value indicates the lower stability limit for the given velocity. Following the elimination process, spacing value reaches a maximum at the same location (meas. 3) and the distribution of spacing along the width of the image follows a Gaussian type of distribution. Afterwards, with the phase-diffusion mechanism, i.e. the movement of triple-point junctions in the lateral direction, the spacing value becomes more

homogeneous, which results in an increase in average eutectic spacing (meas. 4). Lower limit of stability is established by doing many experiments at various velocities and repeating the analysis explained above.

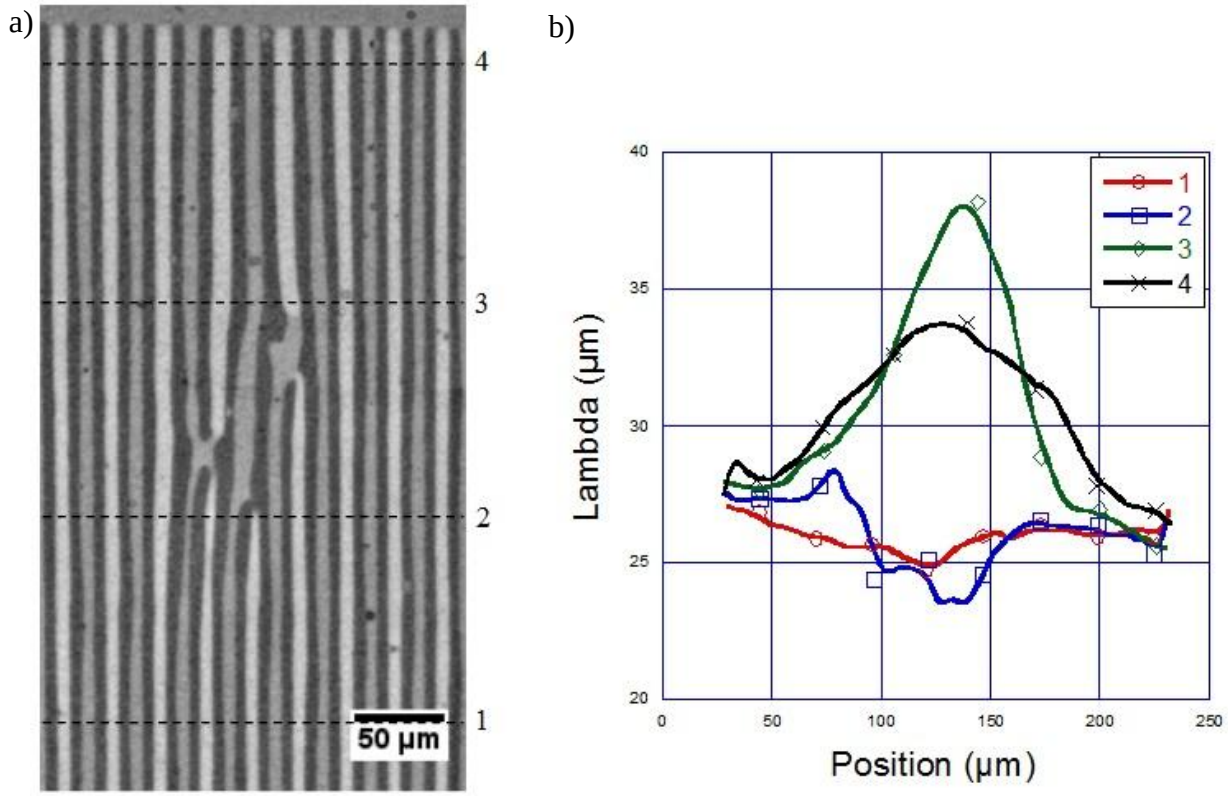

Figure 3.6: a) Elimination process observed when velocity is dropped from 0.27 µm/s to 0.21 µm/s. Growth direction is upwards. b) Eutectic spacing (λ) measurements made before and after elimination from the locations marked as 1, 2, 3, and 4 on the image given in (a) as a function of position in lateral direction; i.e. throughout the width of the image. G = 8 K/mm.

After the establishment of the lower limit, eutectic spacing is forced to go beyond the upper threshold by increasing velocity in order to measure the upper limit of stability. As a result, 1λ oscillation, i.e. oscillations repeating itself in every λ, followed by branching is observed at the upper limit (Fig. 3.7). Although in numerical studies performed using phase-field simulations, various oscillations in three-phased eutectics have been observed [1], this is the first experimental evidence showing that 1λ oscillations can be observed in three-phased eutectics. These oscillations, however, contrary to the ones observed in binary eutectics, are not steady-state structures. They are either damped or amplified, as a result of which the system either goes back to the stable region or branching takes place, respectively.

a) b)

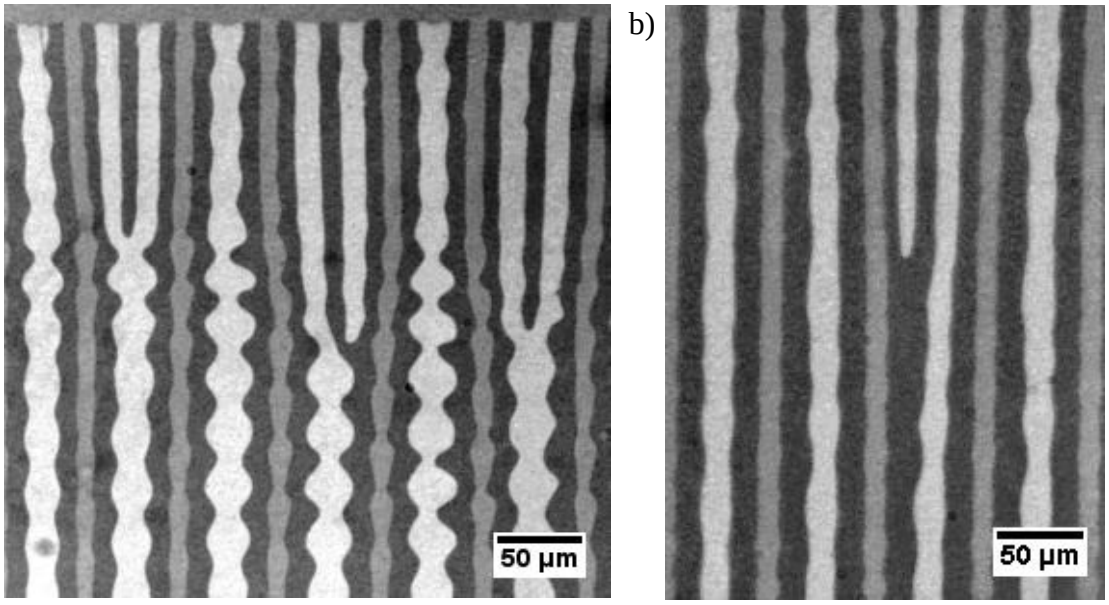

Figure 3.7: Oscillation and branching mechanisms are observed when the system is pushed beyond the upper stability limit as a result of increase in velocity a) from 0.13 µm/s to 0.16 µm/s, b) from 0.099 µm/s to 0.103 µm/s. Growth direction is upwards. G = 8 K/mm.

The recovery of the steady ABAC pattern after the instabilities is found to be dependent on the growth velocity. After elimination process, ABAC pattern is generally recovered quickly especially when the velocity is high. However, ABAC pattern is not obtained back again in a reasonable amount of solidification time after branching. Since branching of all three phases to get back an ABAC pattern is rather difficult in 2D systems, super structures such as ABABAC pattern shown in Fig. 3.8 or even periodic units with higher number of phases can be easily formed by subsequent branching.

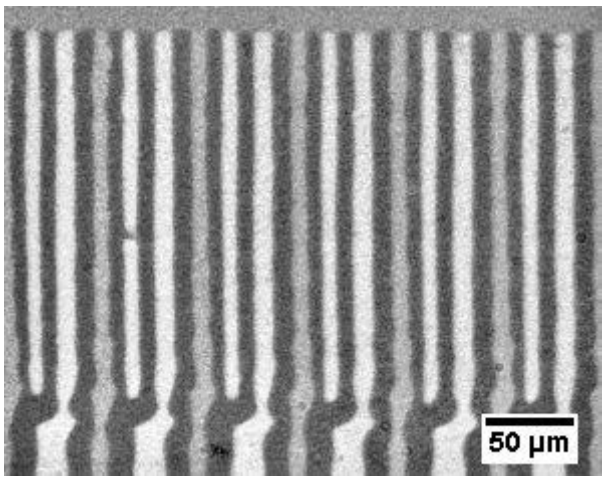

Figure 3.8: ABABAC pattern is formed after branching as a result of V change from 0.113 µm/s to 0.120 µm/s. G = 8 K/mm.

In order to determine the limits of stability, the eutectic spacing is measured at the location just before a spacing adjustment mechanism (elimination, oscillation or branching) is observed. For the lower limit of stability, the minimum eutectic spacing values are measured locally just before an elimination at a given velocity and for the upper limit, maximum eutectic spacing values measured locally just before the branching process. For oscillations, average eutectic spacing values are measured from the oscillating pattern. In Fig. 3.9, eutectic spacing vs. growth velocity is plotted where threshold values for elimination (λ_c), oscillation (λ_{osc}) and branching (λ_{br}) are shown with circles, diamonds, and squares, respectively. Hence, stable growth of ABAC pattern is observed in the region between elimination and oscillation limits. Previous studies of In-Bi-Sn three-phased eutectic system by Witusiewicz et al. and Ruggiero et al. reported $\lambda^2 V$ values by measuring eutectic spacing from stable ABAC patterns [35, 36]. These reported $\lambda^2 V$ values are also plotted in Fig. 3.9 as dashed and dotted lines, which are in complete agreement with the current results since both of the curves lie within the stable spacing range of this study.

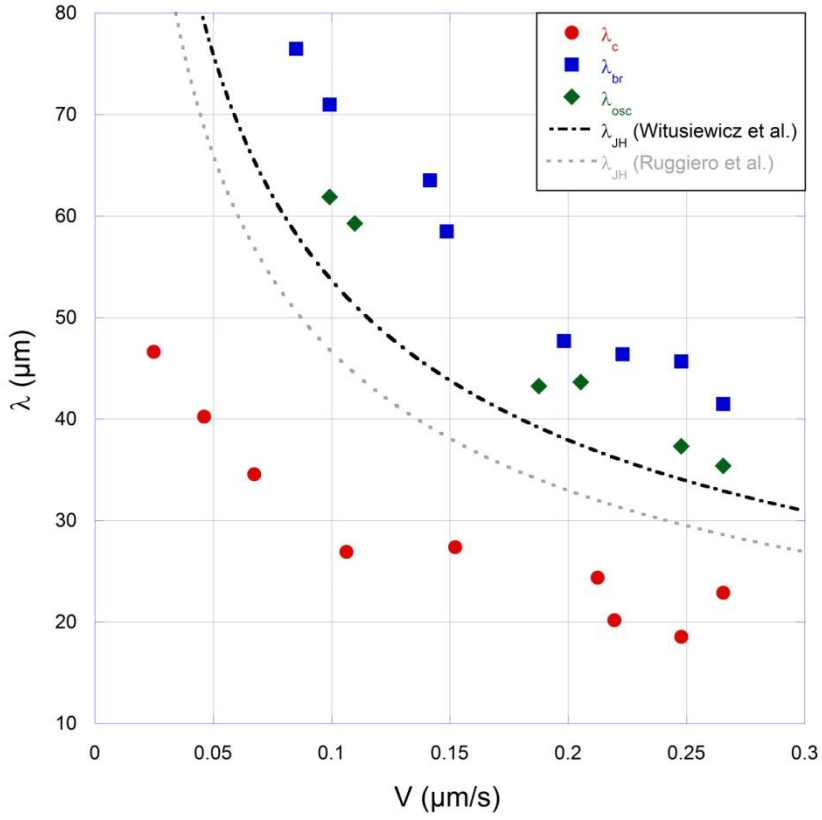

Figure 3.9: The upper and lower limits of stable eutectic spacing (λ) values for ABAC patterns grown at various velocities. Circle, diamond, and square data points indicate the thresholds for elimination, oscillation, and branching spacing adjustment mechanisms, respectively. Dashed and dotted lines: $\lambda^2 V$ values obtained from stable ABAC patterns Witusiewicz et al. and Ruggiero et al., respectively.

Stability measurements taken from tilted patterns are differentiated by using hollow data points in Fig. 3.10 to inspect the effect of tilting on the stability of ABAC pattern. It is concluded that there is no substantial effect of tilted patterns on the stability limits of ABAC pattern since the threshold values of parallel and tilted ABAC patterns are following the same trend. In addition, the measurements from stable growing tilted ABAC pattern (shown with X marks in Fig. 3.10) are found to be in the stable region which supports the deduction regarding the effect of tilted ABAC pattern.

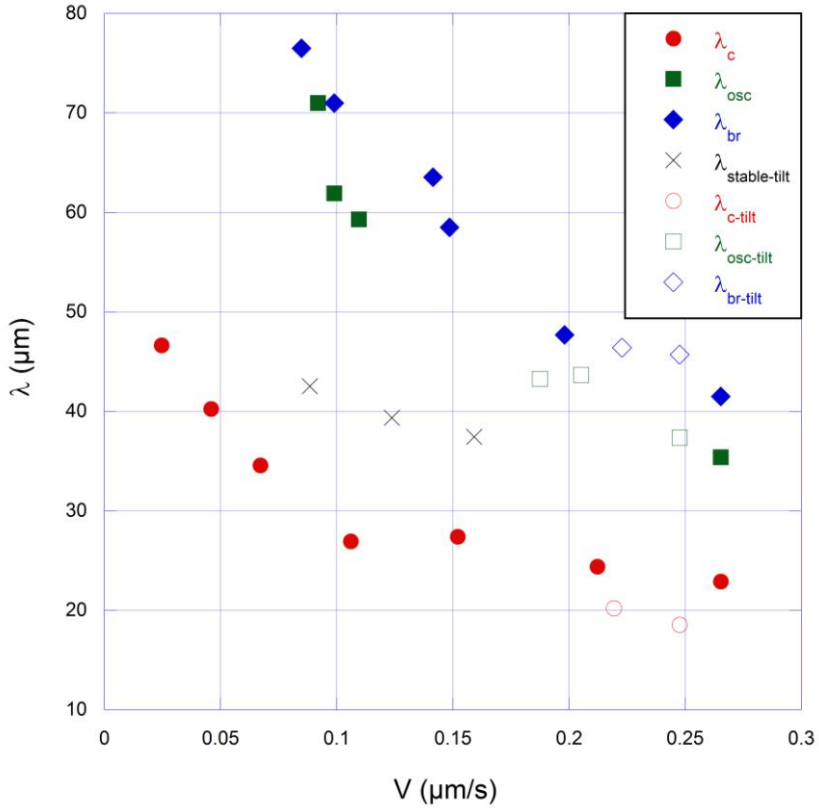

Figure 3.10: Data points indicating the limits of stability for elimination, oscillation, and branching thresholds for parallel and tilted ABAC patterns represented by filled and hollow data points, respectively. Being parallel or tilted is with respect to the thermal gradient direction.

3.3. Determination of Phase Diffusion Coefficient

As mentioned in the section 1.2.1.3, on the contrary to assumption of Jackson and Hunt law, in binary eutectics, triple junctions not only move towards the growth direction, but also can move towards the direction perpendicular to the growth direction [3]. This lateral movement is due to the differences in eutectic spacing of neighboring patterns and achieved by the phase diffusion phenomenon. After the determination of stability thresholds, eutectic spacing distributions, i.e. λ-plots, are measured in order to identify whether the phase

diffusion phenomenon is also valid for three-phased eutectics. Since the difference in the eutectic spacing between neighboring ABAC units would be much higher after an elimination process, the measurements are made in these regions (Fig. 3.6 (b)) and it is showed that phase diffusion also exists in three-phased eutectics.

When λ-modulation along the width of the samples consists of a periodic modulation of amplitude A and wavevector k about an average value λ_0, and if A is sufficiently small and $2\pi k \gg \lambda_0$, the system responses to this perturbation following the Eq. (3.1) [9],

$$\partial_t \lambda(x,t) = D_\lambda \partial_x^2 \lambda(x,t) \qquad (3.1)$$

where t is time and D_λ is the phase diffusion coefficient which shows the amount of triple point junction "diffusion" across a unit area in 1 s. Eq. (3.1) suggests that the amplitude of λ modulation occurs following the Eq. (3.2) where wavevector k is defined as $k = 2\pi/L$ where L is the length of modulation [5].

$$A(t) = \exp(-D_\lambda k^2 t) \qquad (3.2)$$

The data points in the λ-plots generally can be fitted to two different types of distributions, i.e. Gaussian (Normal) or Sinusoidal, depending on the shape of the modulations obtained. When the λ-modulation shows Gaussian type of distribution, which has a solution as in Eq. (3.3), it still verifies Eq. (3.1) giving standard deviation and amplitude evolution as in Eq. (3.4) and Eq. (3.5), respectively.

$$\lambda(x,t) = \lambda_0 + A(t) \exp\left(-\frac{x^2}{\sigma^2}\right) \qquad (3.3)$$

$$\sigma = \sqrt{4D_\lambda (t - t_0)} \qquad (3.4)$$

$$A(t) = A/\sqrt{(t - t_0)} \qquad (3.5)$$

where x is the lateral position, t is time, t_0 is the initial time, λ_0 is the average eutectic spacing, $A(t)$ is the time dependent amplitude value, and σ is the standard deviation.

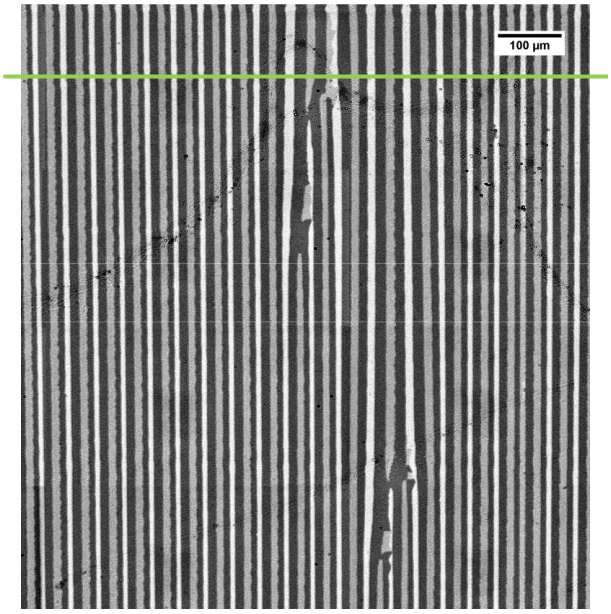

Figure 3.11: ABAC eliminations at V = 0.46 µm/s. Measurements of eutectic spacing for the determination of phase diffusion constant have been made above the green line. G = 8 K/mm.

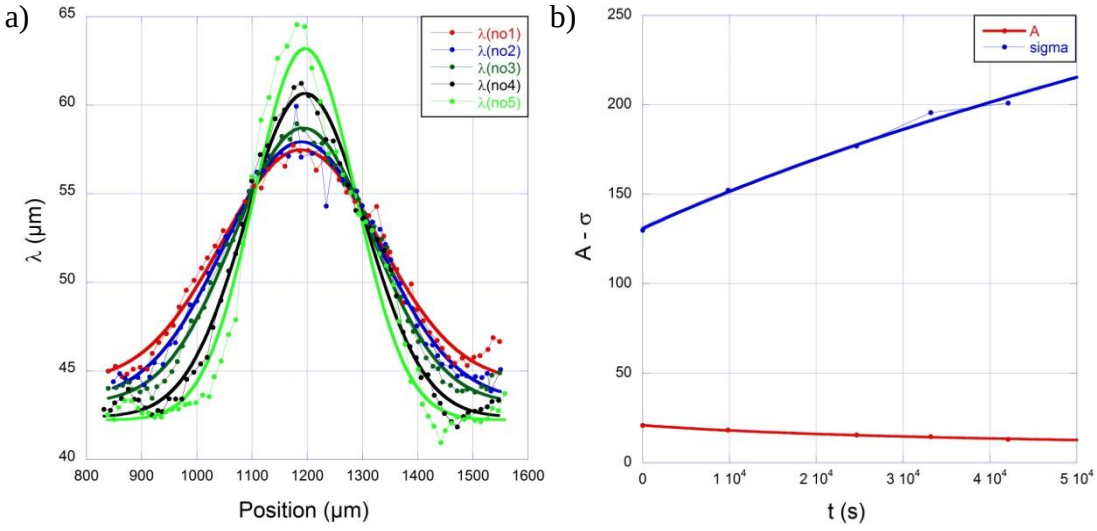

Figure 3.12: a) Eutectic spacing distribution after the second ABAC elimination in Fig. 3.11. Eutectic spacing distribution is Gaussian type and it reaches a maximum (green) right after the elimination process and changes towards homogenization (red) upon further solidification. b) Changes in standard deviation (σ) and amplitude (A) values of Gaussian distribution as a function of time.

In Fig. 3.11, two successive ABAC eliminations are observed and the eutectic spacing distribution changing in time after the second elimination process is plotted in Fig. 3.12 (a). In this case, the measured eutectic spacing data points show Gaussian type of distribution and hence are fitted to Eq. (3.3) as shown in Fig. 3.12 (a). In Fig. 3.12 (b), σ and $A(t)$ as a function

of time are given by fitting the data points to Eq. (3.4) and Eq. (3.5), respectively, and extrapolating the calculations. Since the time difference between measurements and the standard deviations are known, D_λ is calculated by using Eq. (3.4).

In Fig. 3.13, the microstructure of another elimination process is shown. The eutectic spacing measurements taken from this microstructure after the elimination is plotted in Fig. 3.14, where the eutectic spacing distribution shows Sinusoidal type of modulation. The measurements are fitted to the Sinusoidal distribution solution given in Eq. (3.6) where L is the length of the eutectic spacing modulation. Using this equation, $A(t)$ values for each measurement are calculated. Then, knowing the time difference between the formations of microstructures, and hence between the measurements, D_λ is calculated by using Eq. (3.2). D_λ values calculated at different growth velocities and average eutectic spacing values and are tabulated in Table 3.2.

$$\lambda(x,t) = \lambda_0 + A(t)\sin\left(\frac{2\pi x}{L}\right) \quad (3.6)$$

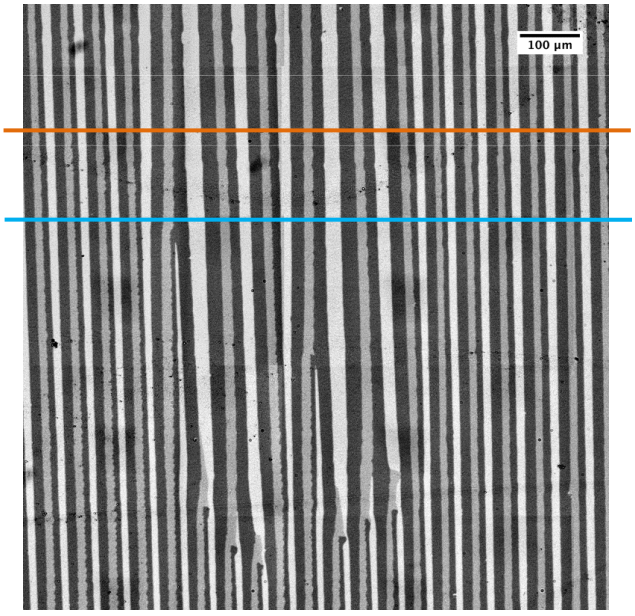

Figure 3.13: ABAC eliminations at V = 0.02 µm/s. Orange and light blue horizontal lines indicate the measurements shown in Fig. 3.14 (a) with same color code (λ (no8), λ (no9)). G = 8 K/mm.

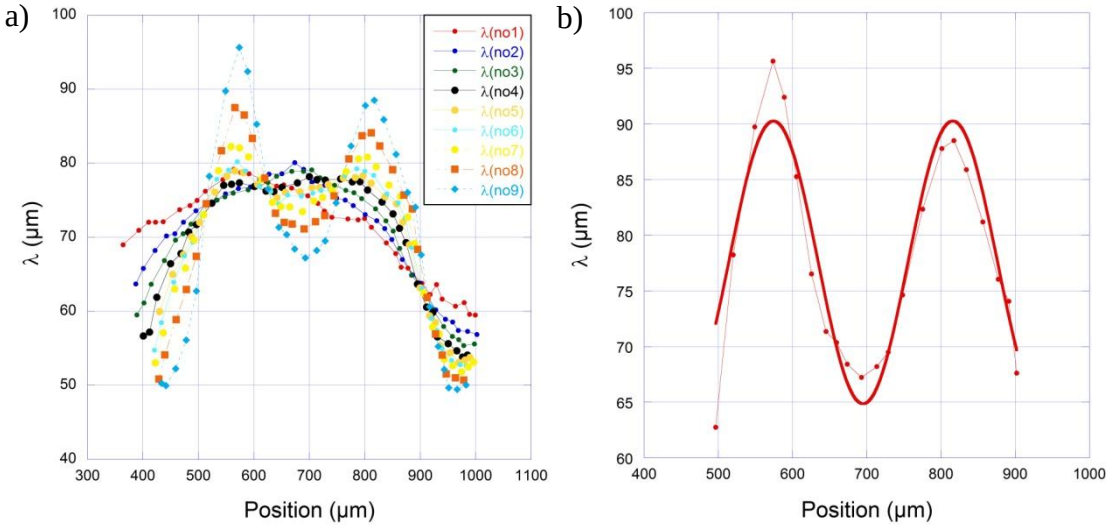

Figure 3.14: a) Eutectic spacing distribution measurements after the ABAC elimination shown in Fig. 3.13. The data points are fitted to the Sinusoidal distribution equation given in Eq. 3.5. After reaching maxima at different locations (light blue) following the elimination process, eutectic spacing homogenizes (red) in time. b) An example fitting of the sinusoidal function (thick curve) to the eutectic spacing distribution measurement λ(no9) in order to calculate amplitude values (*A*).

Table 3.2: Measured values of average eutectic spacing and calculated phase diffusion coefficients at different solidification velocities.

V (μm/s)	λ_0 (μm)	D_λ (μm^2/s)	Distribution
0.025	77.580	0.169	Sinusoidal
0.035	68.400	0.202	Sinusoidal
0.046	49.200	0.146	Gaussian
0.152	36.127	0.847	Sinusoidal
0.212	25.800	0.432	Gaussian
0.495	24.420	7.755	Sinusoidal

3.4. Determination of Jackson and Hunt Constants

Jackson and Hunt constants (K_c, K_r), shown generally as $\lambda_{JH}^2 V$, are extensively used in order to calculate the eutectic spacing of a microstructure that will be obtained at a given velocity before actually doing any solidification experiments. In other words, it defines the scaling parameter for a given eutectic system. In the literature, there are two $\lambda^2 V$ constants reported by Witusiewicz et al. and Ruggiero et al. for In-Bi-Sn three-phased eutectics [35, 36]. These constants are calculated by applying $\lambda^2 V$ fit to the measured eutectic spacing values of stable ABAC patterns. However, $\lambda_{JH}^2 V$ cannot be obtained by fitting any steady-

state measurement of eutectic spacing since it only represents Jackson and Hunt constants at the minimum undercooling spacing values, λ_{JH} or λ_m. Jackson and Hunt (JH) theory states that the undercooling (ΔT) is a function of eutectic spacing and given as:

$$\Delta T(\lambda) = K_r V \lambda + \frac{K_c}{\lambda} \quad (1.1)$$

By taking the second derivative of Eq. (1.1) and equalize it to 0 (ΔT = 0), the minimum undercooling spacing can be calculated, at which JH eutectic spacing is given as:

$$\lambda_m = \lambda_{JH} = \left(\frac{K_c}{K_r V}\right)^{1/2} \quad \text{or} \quad \lambda_{JH}^2 V = \frac{K_c}{K_r} \quad (1.2)$$

The theory of λ-diffusion coefficient for 2D binary lamellar eutectic growth proposed by Langer (Eq. (3.7)) in 1980 [41] predicted that critical eutectic spacing λ_c is equal to λ_{JH}. However, Akamatsu et al. disproved that by showing the eutectic structure remains stable below λ_{JH} and corrected Langer's formula by adding the second term as given in Eq. (3.8) [9]. Here B is defined as a material dependent numerical constant determined empirically, Λ_0 is calculated as $\Lambda_i = \lambda_i / \lambda_{JH}$ and called normalized eutectic spacing value, which simplifies the comparison between different eutectic systems. This equation states that if the value D_λ is lower than 0, the system is unstable; i.e. the differences in eutectic spacing between neighboring units will be amplified with time until a catastrophic change such as elimination or branching occurs. On the other hand, if D_λ is larger than 0, the system is stable; i.e. the system relaxes towards a homogeneous pattern. In order to find the critical value of eutectic spacing (λ_c), which is the elimination threshold in this case, D_λ is equalized to 0.

$$D_\lambda = \frac{K_r \lambda_0 V^2}{G}\left(1 - \frac{1}{\Lambda_0^2}\right) \quad (3.7)$$

$$D_\lambda = \frac{K_r \lambda_0 V^2}{G}\left(1 - \frac{1}{\Lambda_0^2}\right) + BV\lambda_0\Lambda_0 \quad (3.8)$$

JH constants, K_r and K_c, are calculated under the assumption that the given formulas are also applicable for three-phased eutectics. In order to calculate these constants, the data given in Table 3.2 is fitted to Eq. (3.8) with K_c/K_r, K_r/G and B as free parameters. The calculated

constants, namely, K_r, K_c and B, are given in Table 3.3. In binary systems, the estimated relative margin of error due to the measurements is reported as 15% [5]. However, because of the complexity of three-phased systems, grain boundaries in the measurement region, and the measurements taken from the stable pattern (D_λ>0) due to the type of instability, which will be discussed later, the relative margin of error in this study is increased to 25%.

Table 3.3: Calculated Jackson-Hunt constants K_r, K_c and the material parameter B.

$\boldsymbol{K_r}$ $\boldsymbol{(Ks/\mu m^2)}$	$\boldsymbol{K_c}$ $\boldsymbol{(K\mu m)}$	$\boldsymbol{B}$	$\boldsymbol{\lambda_{JH}^2 V}$ $\boldsymbol{(\mu m^3/s)}$
0.0166	2.2255	0.054	135

When the normalized eutectic spacing values (Λ_0) for stable ABAC pattern are calculated using $\lambda_{JH}^2 V$ given in Table 3.3, it is found to be ranging from 0.9 to 1.5. These threshold values are similar to the ones in two-phased eutectics [5, 14, 42]. The upper stability limit is calculated as $\lambda_{br}^2 V = 490\ \mu m^3 s^{-1}$ by fitting $\lambda^2 V$ to the square data points shown in Fig. 3.9, which were measured at locations right before the branching instabilities were observed. The normalized upper limit of spacing is calculated as $\Lambda_{br} = 1.9 \pm 0.5$. For the data points where oscillations are observed, $\Lambda_{osc} \approx 1.6$, but it cannot be taken as a threshold value since the oscillations were never observed to grow for long periods of time, but only are seen as a transitional state between stable and branching patterns.

In order to determine the lower stability limit where ABAC lamellae elimination takes place, D_λ in Eq. (3.8) is equalized to 0 and the resulting equation is given in Eq. 3.9. By using G = 8 K/mm, B and K_r values given in Table 3.3, we get $BG/K_r = 0.026\ \mu\ \mathrm{ms}^{-1}$. Using this value, Λ_c found to be ranging from 0.62 to 1.1 for the velocity range studied in this thesis. The threshold values along with the corresponding fit to the data as well as the $\lambda_{JH}^2 V$ curve are plotted in Fig. 3.15.

$$\frac{BG}{VK_r}\Lambda_c^3 + \Lambda_c^2 - 1 = 0 \qquad (3.9)$$

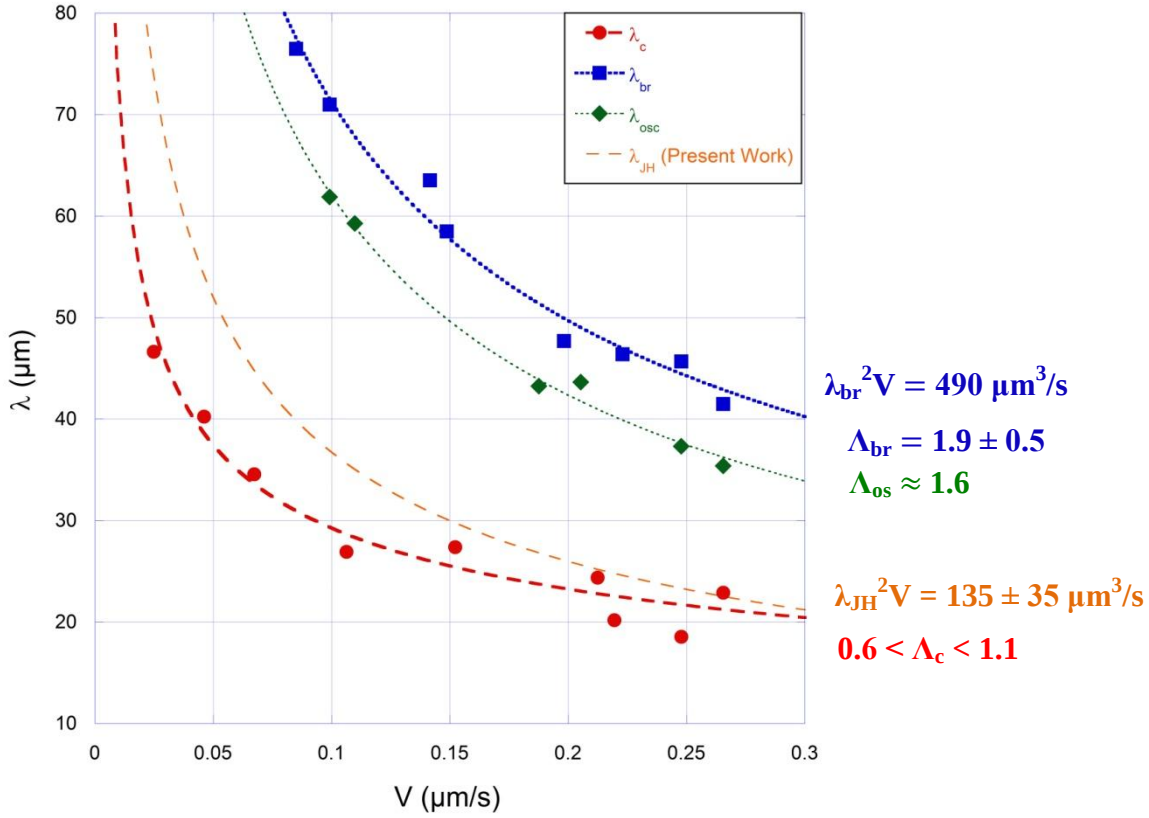

Figure 3.15: Data points of elimination, oscillation and branching instabilities observed in ABAC eutectic structure along with calculated stability limits and Jackson-Hunt constant. Square, diamond and circle shaped data points indicate the limits for elimination, oscillation and branching mechanisms, respectively. Thick dotted line: $\lambda^2 V$ fit to branching data points, thin dotted line: $\lambda^2 V$ fit to oscillation data points, thin dashed line: λ_{JH} curve from the fit of D_λ (Eq. 3.8), thick dashed line: the solution of Eq. 3.9.

The above-reported values are found to be in correspondence with the ones obtained with the two-phased eutectics, especially with In-Bi alloy [5]. However, λ distribution behavior before an elimination process is found to be highly different between two-phased and three-phased eutectics. In two-phased eutectics, there exist a minimum in λ distribution and the amplitude of this minimum exponentially increases in time before the catastrophic event, namely elimination. This type of elimination mechanism observed in two-phased eutectics is called Eckhaus instability. However, in three-phased eutectic microstructures shown in Fig. 3.16 as an example, the modulation of λ distribution before the elimination is not large, i.e. on the order of λ_0 (Fig. 3.17 (a)), and it amplifies very fast as shown in Fig. 3.17 (b). These results indicate that the elimination processes observed are not Eckhaus-type instabilities. In other words, although the elimination takes place in a local minimum value of lambda, lambda distribution is not occurring with a large scale of modulation as in the case of

Eckhaus instability. Moreover, elimination process involves growth termination of four phases in this case, while only one phase is eliminated in Eckhaus instability observed in two-phased eutectics [5]. As a result of phase-field simulations for three-phased eutectic growth of a single ABAC pattern, Choudhury et al. also stated that the termination of a lamella seems to be a different type of instability. In their case, since the whole system is limited to a single ABAC pattern, elimination of one A phase results in a ABC arrangement. They pointed out that the new instability is not a long-wavelength one because it can occur even when only one ABAC pattern is simulated [1]. Note that, they also found the values of eutectic spacing for elimination threshold close to the values of minimum undercooling spacing ($\lambda_c \approx \lambda_{JH}$), which agrees with the results of this study for high values of V as seen in Fig. 3.15. That is, λ_{JH} threshold is found to be close to the lower limit of stability for high growth velocities.

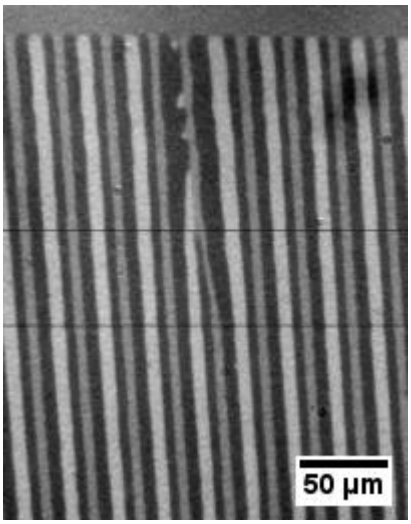

Figure 3.16: The start of an elimination process at V = 0.22 µm/s. G = 8 K/mm.

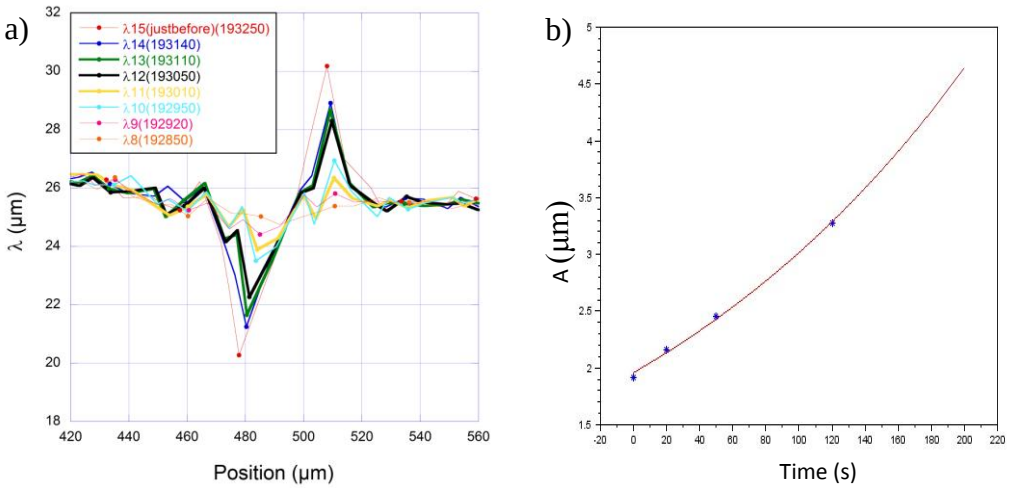

Figure 3.17: a) λ distribution measurements taken before the elimination shown in Fig. 3.16. b) Amplification of λ distribution given in (a) as a function of time.

3.5 Other Microstructural Observations

Throughout the experiments, it is observed that microstructure evolutions may vary depending on cooling rate, process history, defects in the sample, and environmental conditions. For instance, as solidification velocity was dropped substantially from 0.67 μm/s to 0.11 μm/s, In_2Bi phase encapsulated β-In phase by growing on it as shown in Fig. 3.18 (a), which results in a two-phased pattern. In another experiment, a bubble entrapped inside the sample during filling, stopped the growth of the pattern under it and created new surfaces to invade to the neighboring patterns. Continuous branching in this region resulted in a different microstructural arrangement called superstructure, i.e. repeating units of AB and AC forming $[AB]_m[AC]_n$ type of patterns (Fig. 3.18 (b)).

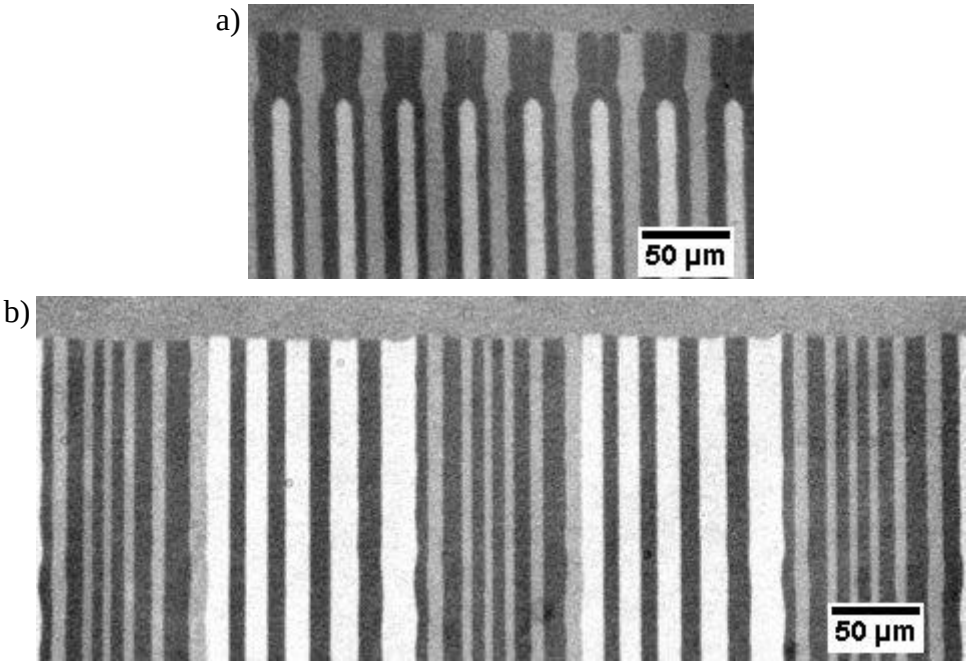

Figure 3.18: Other microstructural arrangements observed in the three-phased eutectic system. a) Encapsulation due to large velocity drop from 0.67 μm/s to 0.11 μm/s, b) Superstructure formed due to a new surface resulted from an air bubble entrapped inside the sample. G = 8 K/mm.

Thickness asymmetry of In_2Bi phases (A phase) in one ABAC pattern is another interesting observation (Fig. 3.19). The phase width ratio of two In_2Bi phases in one ABAC pattern were measured over the width of the image and plotted as a function of time for two different velocities in Fig. 3.20. In Fig. 3.20 (a), elimination of a full ABAC pattern occurs between hour 6 and 8, as a result of which the A1/A2 ratio in that region decreases and that affects the average. Choudhury et al. also observed this type of asymmetry in phase-field simulations where only one ABAC pattern is simulated. The simulation results from their

unpublished work are shown in Fig. 3.21. They have also observed the asymmetry of In_2Bi phases when the growth velocity is decreased as in the case of the current study. Simulations suggest that asymmetry in the system is only a transient which ends with elimination of the thin A phase resulting in ABC pattern. Once 2% anisotropy is added to the crystal/crystal interphases of ABAC pattern in the phase-field model, the asymmetry of In_2Bi phases is found to be stable over longer periods of time, although it transformed to ABC eventually. Observing the thickness asymmetry as a steady-state during long experiments, and knowing from In-Bi binary system that β-In-In_2Bi interphase can be highly anisotropic [43], it is predicted that the main cause of this thickness asymmetry can be the anisotropy of the crystal/crystal interphases. This topic needs further investigation to be clarified.

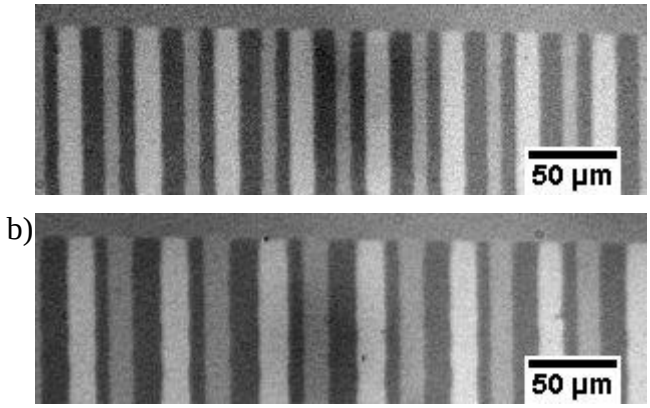

Figure 3.19: Thickness asymmetry of In_2Bi phases in ABAC patterns observed when a) Velocity is dropped from 0.067 µm/s to 0.046 µm/s, b) Velocity is dropped from 0.124 µm/s to 0.071 µm/s. G = 8 K/mm.

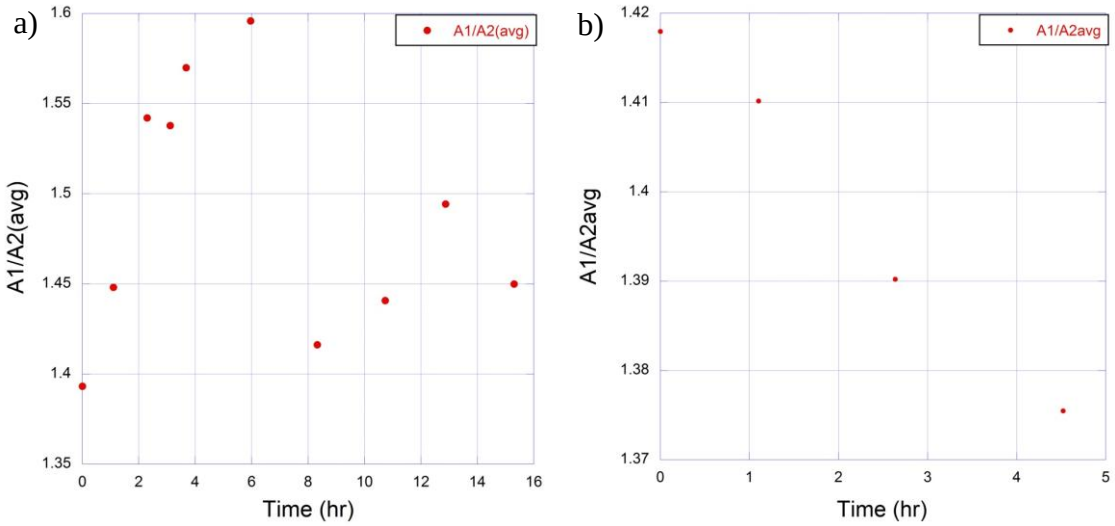

Figure 3.20: The ratio of thick (A1) to thin (A2) In_2Bi phase widths as a function of time. a) V = 0.046 µm/s, b) V = 0.067 µm/s.

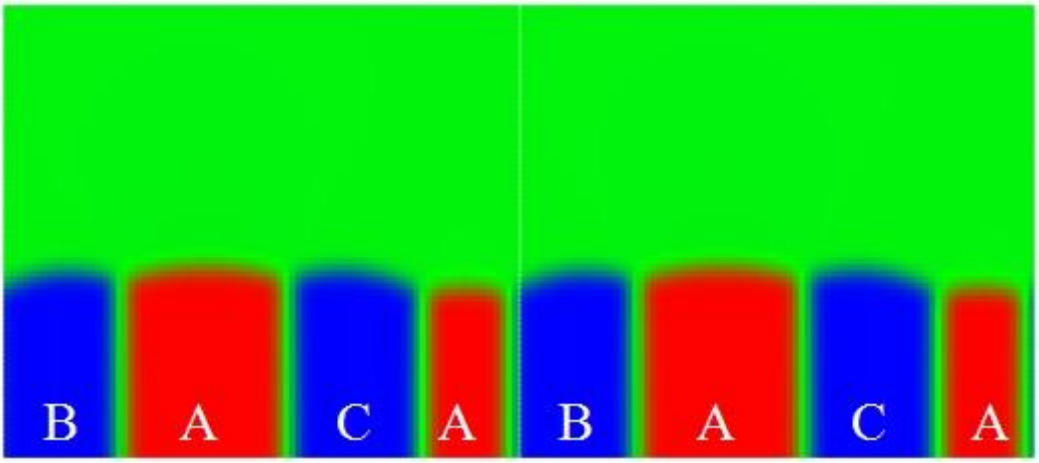

Figure 3.21: Asymmetry observation of A phases in the phase-field simulations by Choudhury et al.

Chapter 4

SUMMARY & CONCLUSIONS

In this thesis, 2D samples of In-Bi-Sn ternary eutectic alloy were directionally solidified using Bridgman technique and the microstructure evolutions were investigated in real-time by an optical microscope. Although in the literature there are two studies about this system, regarding the investigation of the growth dynamics, they were limited to report the microstructures observed and none of them mentioned the stability of these observed patterns. In order to develop the necessary fundamental understanding for the dynamics of three-phased eutectic growth and the stability of three-phased eutectics, many experiments were employed and following conclusions are achieved:

- The solidification of the eutectic alloy led to coupled growth of the three phases with a regular lamellar morphology. The stable microstructure is found to grow with ABAC arrangement of phases, where A, B, and C are In_2Bi, β-In, and γ-Sn phases, respectively. This ABAC order is not only stable in the basic state, but also in tilted and asymmetric patterns.
- When the stable ABAC pattern is perturbed enough by changing the growth velocity, it is forced to go beyond the stability limits and as a result, the system employs spacing adjustment mechanisms like elimination, oscillation, and branching to go back to the stable regime. At the upper and lower stability limits, branching and elimination spacing adjustment mechanisms are observed, respectively. Oscillations were never observed to grow at steady-state, but they were transients that were either amplified and let the system branch or damped so that the system went back to the stable pattern.
- For the determination of stability limits, eutectic spacing measurements were taken right before these instabilities took place at different growth velocities. Branching instability was preceded by 1λO type of oscillation and the upper limit was found to be $\Lambda_{br} = 1.9 \pm 0.5$. The lower limit, Λ_c, was found to be ranging from 0.62 to 1.1 for the velocity range of 0.018 – 1.000 μm/s. These values were found to be in correspondence with the ones obtained with the two-phased eutectics [5, 10, 13]. Eutectic spacing measurements made from stable ABAC pattern performed by previous studies of In-Bi-Sn three-phased

eutectics [35, 36] were in agreement with the results of this study since the $\lambda^2 V$ values reported in those studies are within the stability range of this study.

- The elimination instability observed in three-phased eutectics had a short wavelength mode instead of Eckhaus instability, which is observed in two-phased eutectics after a long-wavelength modulation. Numerical studies by Choudhury et al. [1] also stated that the elimination mechanism in three-phased eutectics is different than Eckhaus instability.
- Measurements taken from ABAC pattern after an elimination process show that the eutectic spacing homogenizes over time by movement of the triple-point junctions in lateral direction, which proves that the phase diffusion is the mechanism responsible for the homogenization of eutectic spacing in three-phased systems, as in the case of two-phased systems. The values of phase diffusion coefficient, D_λ, for the three-phased eutectics are calculated for various velocities employed in this study.
- After the determination of D_λ values, $\lambda_{JH}^2 V$ was calcualted as 135 ± 35 μm^3/s.
- Different microstructures such as tilted ABAC patterns, thickness asymmetry of In_2Bi phases in ABAC patterns, and superstructure were observed depending on cooling rate, process history, defects in the sample, and environmental conditions. Tilted pattern was found to have no substantial effect on the stability limits of ABAC pattern. Both the tilt angle of the tilted patterns and the thickness asymmetry of In_2Bi phases in ABAC pattern are observed to be dependent on growth velocity.

As future work, more thorough research on the instability mode for the lower limit, and the dynamics of thickness asymmetry of In_2Bi phases in ABAC pattern are required for complete understanding of the solidification dynamics of three-phased eutectic patterns. Moreover, this research could be extended to quasi-2D/3D three-phased eutectic patterns and off-eutectic stable patterns. Effect of anisotropy on three-phased eutectic systems is another interesting topic that needs further investigation.

BIBLIOGRAPHY

[1] Choudhury A, Plapp M, Nestler B. Theoretical and numerical study of lamellar eutectic three-phase growth in ternary alloys. Physical Review E. (2011); 83(5).
[2] Jackson KA, Hunt JD. Lamellar and Rod Eutectic Growth. Transactions of the Metallurgical Society of AIME. (1966); 236:1129.
[3] Dantzig JA, Rappaz, M. Solidification. (2009).
[4] Akamatsu S, Faivre G. Anisotropy-driven dynamics of cellular fronts in directional solidification in thin samples. Phys. Rev.E. (1998); 58(3):3302.
[5] Akamatsu S, Bottin-Rousseau S, Faivre G. Determination of the Jackson-Hunt constants of the In-In2Bi eutectic alloy based on in situ observation of its solidification dynamics. Acta Materialia. (2011); 59(20):7586-91.
[6] Imre B. Eutectic system. (2009).
[7] Smith WH, J. Foundations of Materials Science and Engineering (2006).
[8] Akamatsu S, Moulinet S, Faivre G. The Formation of Lamellar-Eutectic Grains in Thin Samples. Metallurgical And Materials Transactions A. (2001); 32A:2039-48.
[9] Akamatsu S, Plapp M, Faivre G, et al. Pattern Stability and Trijunction Motion in Eutectic Solidification. Phys. Rev. (2002); E 66:030501.
[10] Akamatsu S, Plapp M, Faivre G, et al. Overstability of lamellar eutectic growth below the minimum-undercooling spacing. Met. Mat. Trans (2004); 35A:1815-28.
[11] Datye V, Langer JS. Stability of thin lamellar eutectic growth. Physical Review B. (1981); 24(8):4155-69.
[12] Karma A. Beyond Steady-State Lamellar Eutectic Growth. Physical Review Letters. (1987); 59(1):71.
[13] Akamatsu S, Bottin-Rousseau S, Perrut M, et al. Real-time study of thin and bulk eutectic growth in succinonitrile-(d)camphor alloys. Journal of Crystal Growth. (2007); 299(2):418.
[14] Karma A, Sarkissian A. Morphological instabilities of lamellar eutectics. Metall. Mater. Trans. A-Phys. Metall. Mater. Sci. (1996); 27(3):635-56.
[15] Witusiewicz VT, Sturz L, Hecht U, et al. Phase equilibria and eutectic growth in quaternary organic alloys amino-methyl-propanediol-(D)camphor-neopentylglycol-succinonitrile (AMPD-DC-NPG-SCN). Journal of Crystal Growth. (2006); 297(1):117-32.
[16] Hecht U, Granasy L, Pusztai T, et al. Multiphase solidification in multicomponent alloys. Mater. Sci. Eng. R-Rep. (2004); 46(1-2):1-49.
[17] Fisher DJ, Kurz W. Novel Morphology Of Pb-Sn-Cd-Zn Quaternary Eutectic. Metallurgical Transactions. (1974); 5(6):1508-10.
[18] Gregory LG, Dunne DP, Delamore GW. Crystallographic orientation relationships in the tin-lead-cadmium ternary eutectic. J. Mater. Sci. (1983); 18(1):51-6.
[19] Ruggiero MA, Rutter JW. Formation of microstructure during solidification of Bi-Pb-Sn ternary eutectic. Materials Science And Technology. (1999); 15(10):1110-4.
[20] Snugovsky L, Perovic DD, Rutter JW. Microstructures formed by directional solidification of two ternary eutectic alloys of Bi-Cd-In system. Materials Science and Technology. (2000); 16(9):979-83.
[21] Lee JH, Yoshikawa A, Fukuda T, et al. Growth and characterization of Al2O3/Y3Al5O12/ZrO2 ternary eutectic fibers. Journal of Crystal Growth. (2001); 231(1-2):115-20.
[22] Grobner J, Kevorkov D, Chumak I, et al. Experimental investigation and thermodynamic calculation of ternary Al-Ca-Mg phase equilibria. Zeitschrift Fur Metallkunde. (2003); 94(9):976-82.

[23] Rios CT, Milenkovic S, Caram R. A novel ternary eutectic in the Nb-Al-Ni system. Scripta Materialia. (2003); 48(10):1495-500.
[24] Moon KW, Boettinger WJ. Accurately determining eutectic compositions: The Sn-Ag-Cu ternary eutectic. Jom. (2004); 56(4):22-7.
[25] Rios CT, Oliveira MF, Caram R, et al. Directional and rapid solidification of Al-Nb-Ni ternary eutectic alloy. Materials Science And Engineering A-Structural Materials Properties Microstructure And Processing. (2004); 375-77:565-70.
[26] Snugovsky L, Perovic DD, Rutter JW. Solidification of ternary eutectic and near eutectic alloys in the Ag-Cu-Sn system. Materials Science And Technology. (2004); 20(11):1403-13.
[27] Sturz L, Witusiewicz VT, Hecht U, et al. Organic alloy systems suitable for the investigation of regular binary and ternary eutectic growth. Journal of Crystal Growth. (2004); 270:273-82.
[28] Wilde De J, Froyen L. Microstructures observed during directional solidification along the univariant eutectuc reaction in a ternary al-cul-si alloy. Materials Science Forum. (2006); 508:51-6.
[29] Witusiewicz VT, Hecht U, Sturz L, et al. Phase Equilibria and eutectic growth in ternary organic system (D) Camphor-Neopentylglycol-Succinonitrile. Journal of Crystal Growth. (2006); 286:431-9.
[30] Witusiewicz VT, Hecht U, Sturz L, et al. Phase equilibria and eutectic growth in ternary organic system amino-methyl-propanediol-(D)camphor-neopentylglycol. Journal of Crystal Growth. (2006); 286(1):137.
[31] Contieri RJ, Rios CT, Zanotello M, et al. Growth and three-dimensional analysis of a Nb-Al-Ni ternary eutectic. Mater. Charact. (2008); 59(6):693-9.
[32] Kattner UR, Boettinger WJ. Thermodynamic Calculation of the Ternary Ti-Al-Nb System. Materials Science and Engineering. (1992); A152:9-17.
[33] Rex S, Bottger B, Witusiewicz V, et al. Transient eutectic solidification in In-Bi-Sn: Two-dimensional experiments and numerical simulation. Materials Science And Engineering A-Structural Materials Properties Microstructure And Processing. (2005); 413:249-54.
[34] Boettinger WJ. Surface Relief Cinemicrography of the Unsteady Solidification of the Lead-Tin-Cadmium Ternary Eutectic: The Johns Hopkins University; 1972.
[35] Witusiewicz VT, Hecht U, Rex S, et al. In situ observation of microstructure evolution in low-melting Bi-In-Sn alloys by light microscopy. Acta Materialia. (2005); 53(13):3663-9.
[36] Ruggiero MA, Rutter JW. Origin of microstructure in the 332 K eutectic of the Bi-In-Sn system. Materials Science and Technology. (1997); 13(1):5-11.
[37] Genau AL, Ratke L. Crystal orientation and morphology in Al-Ag-Cu ternary eutectic. Iop Conf Ser-Mat Sci. (2012); 27.
[38] Abtew M, Selvaduray G. Lead-free Solders in Microelectronics. Materials Science and Engineering: R: Reports. (2000); 27(5–6):95-141.
[39] Witusiewicz VT, Hecht U, Bottger B, et al. Thermodynamic re-optimisation of the Bi-In-Sn system based on new experimental data. Journal of Alloys and Compounds. (2007); 428(1-2):115-24.
[40] Akamatsu S, Bottin-Rousseau S, Serefoglu M, et al. A theory of thin lamellar eutectic growth with anisotropic interphase boundaries. Acta Materialia. (2012); 60(6-7):3199-205.
[41] Langer JS. Eutectic Solidification and Marginal Stability. Phys. Rev. Letters. (1980); 44(15):1023.
[42] Ginibre M, Akamatsu S, Faivre G. Experimental Determination of the Stability Diagram of a Lamellar Eutectic Growth Front. The American Physical Society- Physical Review E. (1997); 56(1):780.

[43] Akamatsu S, Bottin-Rousseau S, Serefoglu M, et al. Lamellar eutectic growth with anisotropic interphase boundaries: Experimental study using the rotating directional solidification method. Acta Materialia. (2012); 60(6-7):3206-14.